Melt percolation, concentration and dyking in the Hawaiian mantle plume and overriding lithosphere: links to the evolution of lava composition along the volcanic chain

Azam Soltanmohammadi, Michel Grégoire, Fabrice J Fontaine, L Paul Bédard, Marc Blanchard, Michel Rabinowicz

OXFORD UNIVERSITY PRESS | Journal of Petrology

Draft Manuscript for Review

Melt percolation, concentration and dyking in the Hawaiian mantle plume and overriding lithosphere: links to the evolution of lava composition along the volcanic chain

Journal:	*Journal of Petrology*
Manuscript ID	JPET-Sep-20-0123.R3
Manuscript Type:	Original Manuscript
Date Submitted by the Author:	28-Nov-2021
Complete List of Authors:	Soltanmohammadi, Azam; Geosciences Environnement Toulouse, Observatoire Midi-Pyrénées; Université du Québec à Chicoutimi, Centre d'étude sur les Ressources minérales (CERM), Sciences de la Terre & LabMaTer Gregoire, Michel; Geosciences Environnement Toulouse, Observatoire Midi-Pyrénées Fontaine, Fabrice; Observatoire du Piton de la Fournais Bédard, L.Paul; Université du Québec à Chicoutimi, Centre d'étude sur les Ressources minérales (CERM), Sciences de la Terre & LabMaTer Blanchard, Marc; Geosciences Environnement Toulouse, Observatoire Midi-Pyrénées Rabinowicz, Michel; Geosciences Environnement Toulouse, Observatoire Midi-Pyrénées
Keyword:	meimechite, kimberlite-like melt, oceanic island alkali basalts, Hawaiian plume, heterogeneous mantle, melt percolation

Melt percolation, concentration and dyking in the Hawaiian mantle plume and overriding lithosphere: links to the evolution of lava composition along the volcanic chain

Azam Soltanmohammadi[1,2*], Michel Grégoire[1], Fabrice J. Fontaine[3], L. Paul Bédard[2], Marc Blanchard[1], Michel Rabinowicz[1]

[1] Géosciences Environnement Toulouse (GET), Observatoire Midi-Pyrénées, Université Paul Sabatier Toulouse III-CNRS-CNES-IRD, Toulouse, France; [2] Centre d'étude sur les Ressources minérales (CERM), Sciences de la Terre & LabMaTer, Université du Québec à Chicoutimi, Chicoutimi, Québec, Canada; [3] Observatoire du Piton de la Fournais, La Réunion Island

*Corresponding author. Email: azamsoltanmohammadi@gmail.com

ABSTRACT

Oceanic island basalts and related magmatic rocks from Hawaii are derived from a compositionally heterogeneous mantle plume. Here we describe how this heterogeneity results from the transport of filaments of a specific composition in the plume, representing a relatively small volume of rocks (~15%) interbedded inside a dry peridotite mantle. Four types of filaments are considered: sub-primitive mantle, ultra-low-velocity zone, fertilized-harzburgite and eclogite type filaments. We present a model that describes the flow within a plume and the stress field in the overriding viscoelastic lithosphere and that can determine, from depth to the surface, the melting rate, composition and trajectory of melts produced within each type of filament. Our model shows that (i) the filaments melt at a depth greater than 5 GPa, where the temperature gap between the solidus and liquidus is narrow (~ 40°C to 80°C), and (ii) the volume of filaments is small relative to the total volume of mantle, which therefore allows the latent heat required for the partial melting to be provided via conduction inside the hot plume.

The primitive melts produced inside the filaments, occasionally mixed with the melt derived from an eclogite filament, represent a volume comparable with that expected in a plume composed only of dry peridotite that partially melts to a degree of ~10% at the interface between the spinel and garnet fields (60–70 km depth). In particular, in the centre of the plume, sub-primitive mantle filaments produce up to 30% tholeiite-picrite melts, whereas in fertilized-harzburgite filaments, the mantle melts completely to produce a melt having a meimechite-like composition. A key finding is that the fractional crystallization of these melts likely forms the so-called "primary mantle–derived alkaline magmas" along with dunites and olivine-rich cumulates. Our plume model shows that the mantle flow divides into two parts. The first corresponds to hot flowlines that originate at a depth of ~200 km and at a distance of less than 25 km from the plume axis. Along these flowlines, when the mantle reaches a pressure of 5 GPa, the partially molten horizon in filaments is sufficiently thick for the interstitial melt to be squeezed out via dykes. This melt eventually ponds as sills in a subrectangular zone that is located inside the overlying lithosphere, between 70 and 50 km depth and centred over a distance of less than 40 km on either side of the axis. This zone is designated as the shield magmatic reservoir. The volatile-rich melt inside the sills infiltrates the surrounding mantle lithosphere and partially melts it. After ~0.1 Ma, the melt resumes its vertical ascent via dykes and eventually ponds and differentiates within subcrustal magma chambers located below active shield volcanoes. This sequence of processes matches the expected volume, petrology and geochemistry recorded for shield volcanoes. The second part of the melt flow does not pond within the shield magmatic reservoir. Rather, the mantle cold flowlines, originating at ~200 km depth and at 25 to 35 km from the plume axis, discharge their interstitial melt through dykes that were initially generated deeper, at ~5 GPa. The melt reaches the Moho at 100 to 150 km from the plume axis, where it forms magmatic bodies within which the melt differentiates. This melt likely represents that observed in pre- and postshield volcanoes. Finally, at ~70 km from

the plume axis and at a depth greater than 200 km, the flowlines are subvertical. They then deflect at ~180 km depth and rotate toward the horizontal and eventually transit at 10° to 20° to the horizontal across a ~200 km distance from the axis and reach ~140 km depth. The fertilized-harzburgite and sub-primitive mantle/ultra-low-velocity zone filaments that flow along these elbows partially melt by a few to several percent. The resulting interstitial melt has a kimberlite-like composition. Thereafter, the excess pressure at the top of the filament at ~200 km from the axis overcomes the threshold for dyking and thus allows the escape of the interstitial melt via dykes ponding in subcrustal magma chambers or emerging directly at the surface. These melts have a composition similar to that associated with rejuvenated volcanism. We use the nature and the composition of whole erupted magmas and the seismic structure along the Hawaiian chain to validate this model.

KEYWORDS: meimechite, kimberlite-like melt, oceanic island alkali basalts, Hawaiian plume, heterogeneous mantle, melt percolation

INTRODUCTION

The long-standing debate regarding the origin of oceanic island basalts (OIBs) remains largely unresolved. In particular, melting processes (pressure, temperature and degree of melting) fail to explain the full spectrum of petrological and geochemical characteristics of Hawaiian magmas. This failure stems from the mantle being composed of streaks of material, which we designate here as "*filaments*". These filaments are transported by mantle convection and differ in their lithologies and volatile contents (e.g. Farnetani & Hofmann, 2010; Hofmann *et al.*, 2011). Accordingly, these materials partially melt at different depths and temperatures, and the resulting interstitial melts percolate within the mantle and eventually escape through fast-propagating dykes before ponding at various depths (Spera, 1987; Grégoire *et al.*, 2006; Soltanmohammadi *et al.*, 2018). Moreover, the interaction of the ponded melts with the

surrounding rocks gives rise to new streaks that produce the specific petrological and geochemical signatures of the resulting magmas. Recent progress in the modelling of mantle convection, together with plate tectonics, has advanced the understanding as to how the most important lithological and compositional streaks form within the mantle and then partially melt at depth (e.g. Farnetani & Hofmann, 2010; Hofmann *et al.*, 2011; Ballmer *et al.*, 2013). In contrast, the modelling of melt percolation, migration and concentration within the various streaks during convective transport remains limited. Here we link the nature and composition of erupted magmas along the Hawaiian chain and present more precise melt migration models. Our models lead to reliable quantitative explanations for the final composition of the various Hawaiian magmas. In this paper, we consider the following types of filament and mantle reservoirs:

"Eclogitic" and *"fertilized*-harzburgite *filaments"*: A commonly invoked paradigm of both geochemistry and geodynamics is that subduction processes have a major effect on the evolution of mantle composition, in particular for magmas originating from intraplate volcanism (e.g. Sobolev *et al*., 2005). This paradigm relates to the melting processes and solid-phase changes during subduction that transform subducting crust—mostly oceanic, but also some continental crust—and the associated sediments into eclogites *sensu lato* at >100 km depth (e.g. Gill, 1981; Hacker *et al*., 2003). These ~5 km thick eclogite layers ultimately detach from the previously attached mantle portion of the lithosphere (e.g. Rüpke *et al*., 2004). A ~30 km thick layer of serpentinites produced during hydrothermalism at the ridge crest along major faults and during plate bending prior to subduction are transformed at depth into harzburgite and are refertilized, in particular by volatile and alkaline elements (Elthon, 1992; Ross *et al.,* 2005; Faccenda, 2014; DeFelice *et al*., 2019). We refer to these subduction-derived recycled serpentinites as fertilized harzburgite, possibly associated with recycled non-serpentinized oceanic peridotites or mantle wedge–related peridotites and serpentinites. Both the eclogites

and the fertilized harzburgites are particularly stable through the lower mantle, but become unstable when convection returns them to the upper mantle within or above the mantle transition zone (MTZ) (e.g. Hirschmann, 2006; Motoki & Ballmer, 2015; Soltanmohammadi *et al*., 2018).

"Sub-primitive mantle filament": The preservation of primitive mantle geochemical signatures, e.g. high He^3/He^4 values and $\mu^{182}W$ ~0 (Mundl-Petermeier *et al.*, 2020), of some plume-derived lavas (e.g. OIBs) provide evidence for the existence (survival) of a primitive mantle reservoir. This mantle reservoir is believed to be in the lower mantle. It eventually penetrates the upper mantle via deep-rooted mantle plumes (Courtillot *et al.*, 2003; McNamara, 2019). In this text, we designate this reservoir as the sub-primitive mantle reservoir. In particular, the sub-primitive mantle reservoir used in this study has a lherzolite-like composition but is considered relatively rich in volatile, alkaline and incompatible elements. Moreover, the geochemical signature indicates this reservoir was never processed by melting or degassing after the formation of the Earth's core (e.g. Kurtz *et al*., 1983; Collerson *et al.*, 2010; Mundl-Petermeier *et al.*, 2020). The presence of a sub-primitive mantle reservoir indicates that the convective processes that tend to homogenize the entire Earth mantle did not affect this reservoir. This idea is supported by seismic tomography that shows the mantle convective plumes in the lower mantle being very broad; thus, the viscosity in the lower mantle is several orders of magnitude greater than that within the upper mantle. The convective velocities are therefore reduced in the lower mantle (French & Romanowicz, 2015; Liu *et al*., 2018). Consequently, the overturn time of convection for an entire mantle cell represents ~1 Ga, and a large volume of the lower mantle stagnates mainly inside the several 1000 km wide interior of these convective cells, thereby preventing the mechanical homogenization of the sub-primitive mantle with dry peridotite. Eventually, the shear at the borders of the plume entrains some sub-pristine mantle inside the whole-mantle convection into the main plume flow. This process forms a sub-primitive filament having a thickness

123 comparable to the vertical dynamic boundary layer surrounding the mantle plume, i.e. a few
124 to several tens of kilometres (Farnetani *et al*., 2002)**.**

125 *"ULVZ filament*": Seismic wave reflection along the core-mantle interface shows the presence
126 of patchy ultra-low-velocity zones (ULVZs) (Li *et al.*, 2017). These zones are thin (~5–40 km
127 thick and several hundred kilometres wide) and are generally found near or within large low-
128 seismic-velocity provinces (LLSVPs). These provinces represent the ~500 km thick hot
129 boundary layer of whole-mantle convection, a layer that contains the roots of various plumes
130 set below the two antipolar African and Central Pacific superswells (French & Romanowicz,
131 2015, McNamara *et al*., 2019). Because mantle flow along the core converges toward the axis
132 of the plume, the ULVZs pile up near the root of the plume as the hottest region in the lower
133 mantle. Accordingly, the ULVZs are linked to partial melting. As similar structures—
134 although having lower S-velocities—have also been detected well outside LLSVPs,
135 particularly beneath subduction zones, it is thought that the ULVZs are not only partially
136 melted but also compositionally heterogeneous, i.e. consist of eclogite and/or volatile-rich
137 mantle (Collerson *et al*., 2010; Andrault *et al*., 2014; Nomura *et al*., 2014). In addition, some
138 volatiles and metals are directly provided to the mantle by the core. This is the case for CO_2
139 (Collerson *et al.*, 2010; Dobretsov & Shatskiy, 2012), He (showing an elevated $^{3}He/^{4}He$
140 ratio), and also evidenced by highly negative $\mu^{182}W$ (Mundl-Petermeier *et al.*, 2020), Fe (Mao
141 *et al.*, 2017) and ^{186}Os (Brandon *et al*., 1999). In short, all necessary conditions for developing
142 ULVZ filaments are achieved at the root of the Hawaiian plume. These filaments are likely
143 entrained upward by the plume and eventually solidify well above the core-mantle interface
144 (Collerson *et al.*, 2010). This process would form solid volatile-rich filaments having a
145 lherzolite-like composition with an elevated $^{3}He/^{4}He$ ratios and a $\mu^{182}W < 0$. These filaments
146 are thereafter propelled upward by the plume flow (Farnetani *et al.*, 2018). As we do not have
147 more quantitative information related to the true composition of the ULVZ filament, we

assume that it contains the same volatile content and $^{3}He/^{4}He$ ratio as a sub-primitive mantle filament.

"The ambient mantle": A well-accepted paradigm is that the upper mantle is mostly depleted, thought to represent the mechanically homogenized MORB mantle reservoir (Harpp & Weis, 2020). According to these authors, the Hawaiian plume pushes it apart to collide with the lithosphere. Nonetheless, the model does not indicate what occurs after more than 100 Ma of quasi-steady life of the plume when a huge volume of the MORB dry mantle reservoir, representing the volume of a ~2000 km section (assuming that the ascending velocity of the plume at the upper mantle/lower mantle interface is 10 cm/yr), has been driven back into the lower mantle. To address this problem, we can first turn to the case of the Asian continent, which is surrounded by oceanic plates including the Pacific. An oceanic plate does not penetrate inside the lower mantle and eventually floats along the MTZ below the China block up to 2000 km distant from the Japan arc. There, it is highly likely that the upper convective mantle remained isolated from the lower convective mantle during an orogeny, i.e. during ~200 Ma (Agrusta, *et al*., 2017). Then, because the upper-mantle convection is much faster than that of the lower mantle (~10 cm/yr), the overturn time for convection takes only ~20 Ma. After ~200 Ma it has therefore overturned 10 times, sufficient to mechanically homogenize both eclogites and fertilized harzburgites to eventually attain a centimetre-scale size (van Keken *et al*., 2003). The marble-cake model, used to explain the formation of several centimetre-thick pyroxenite bands, supports this paradigm (Allegre & Turcotte, 1986). This model leads to the idea of a specific composition of a fully homogenized mantle low in volatiles and other incompatible elements, sometimes designated as the DMM (depleted MORB mantle). In this text, we name it the "dry peridotite" reservoir. Although, at present, the stratification of convection on both sides of the mantle appears relatively exceptional, it does likely still occur beneath both the west coast of the United States (Rigo *et al*. 2015) and

the central Atlantic (Courtillot *et al.*, 2003). It is suspected, however, that before 3 Ga, layering was systematic (Breuer and Spohn, 1995). The key problem is to determine what happened after 3 Ga when the lower mantle flushed inside the upper mantle (i.e. Breuer & Spohn, 1995). Given the data considered in this study, it is likely that borders of the entire mantle convective cell, e.g. the Hawaiian case, are constituted of dry peridotite, i.e. the axis of the plume, the cell top below the lithosphere, the vertical return flow in the mantle and along the cell bottom above the core. Finally, the cylindrical interior of the convective cell must contain an essential volume of primitive mantle. In this context, the dry peridotitic border of the entire mantle convection cell constitutes the envelope in which the eclogite, fertilized-harzburgite, sub-primitive mantle and ULVZ filaments circulate. In particular, these filaments all converge toward the axis of the Hawaiian plume where they rise inside the plume towards the sublithospheric mantle.

The aim of our paper is to detail what happens to these filaments when they partially melt. The present model agrees well with the latest geochemical conception of the Hawaiian plume. For instance, the main large-scale heterogeneity of the shield magmatism, representing by far the largest volume of Hawaiian magmas, is demonstrated by the compositional differences of lava sources for volcanoes located along a line linking Loihi and Kauai (Loa trend line) and those located along a line joining Kilauea to East Moluka'i (Kea trend line) (e.g. Dana, 1849; Appleman and Dana, 1987; Frey *et al*., 2016). The radiogenic isotopic ratios of most Hawaiian volcanoes indicate that the Loa- and Kea-type mantles originate from two geochemically distinct deep mantle reservoirs (Weis *et al*., 2011; Harrison *et al.*, 2017; Weis *et al*., 2020). The Loa-type reservoir is proposed to originate from the central Pacific LLSVP, particularly rich in ULVZ filaments, whereas the Kea-type reservoir originates from the "Pacific mantle," away from the LLSVP (see Fig. 5 of Weis *et al*., 2011; Fig. 4 of French and Romanowicz, 2015; Fig. 4 of Harrison *et al*., 2017; and Fig. 5 of Weis *et al*., 2020). Note that

for these authors, the Pacific mantle likely represents the relatively cold, ~500 km thick, bottom flow that transports eclogite, fertilized-harzburgite and sub-primitive mantle filaments toward the axis of the Hawaiian plume set along the border of the central Pacific LLSVP. They consider that the geochemical characteristics of each volcano are a direct fingerprint of a specific filament, whereas our approach holds that the Hawaiian lavas are derived from various filaments and from the melts' percolation, ponding/mixing and interaction with the surrounding mantle and/or overriding lithosphere.

Because of the thick lithosphere overlying the Hawaiian plume, partial melting of the dry peridotite inside the plume is limited if it occurs at all (as will be discussed below). In the Hawaiian context, this indicates that the primitive melts of Hawaii do not originate from a normal dry mantle. Therefore, it implies that even in the hot centre of the plume, the mantle must contain a notable quantity of volatiles to partially melt (Wallace, 1998; Putirka, 1999; Li *et al*., 2000). Further, the composition of some metasomatized sources indicates that the sources originate either from fertilized harzburgite (Dawson *et al*., 1980; Grégoire *et al*., 2002) or from the sub-primitive mantle (Collerson *et al*., 2010). Estimates of the volatile content of the fertilized-harzburgite and sub-primitive-mantle components of the Hawaiian plume range from 450 ppm to 750 ppm for H_2O and up to 1300 ppm for CO_2 (Dixon *et al*., 1997; Wallace, 1998; Marty, 2012; Tucker *et al*., 2019). Therefore, inside the lower mantle, the interstitial H_2O concentrates in dense hydrous magnesium silicate phases (DHMS), and CO_2 is reduced to carbide or diamond. When the mantle migrates up within the centre of the plume and crosses the interface between the lower and upper mantle, its temperature is very high, likely ranging between 1800°C and 2100°C (Liu *et al*., 2018). The DHMS, i.e. phases D and B identified as holding most of the water in the deep mantle, therefore melt (Ringwood and Major, 1967; Liu, 1987; Gasparik, 1993; Ohtani *et al.*, 2001). In addition, during the ascent of the plume within the horizon lying between the ringwoodite-perovskite and the garnet-perovskite phase

transitions, the production of majorite likely leads to the oxidation of C (Stagno & Frost, 2010; Kiseeva *et al*., 2018). Because the melting temperature of the carbonates at these depths is less than 1800°C to 2100°C, we deduce that a H_2O- and CO_2-rich melt is produced inside the garnet-perovskite transition zone. The plume model of Ballmer *et al.* (2013) suggests that the mantle plume flow contains 15% and ~20% of eclogite and hydrated lherzolite filaments, respectively, to explain the produced crust volume and the distribution of the volcanoes along the Hawaiian chain. Furthermore, this model assumes that the eclogite transported by the Hawaiian plume melts at a pressure of ~5 GPa (~150 km depth) and then infiltrates the surrounding peridotites to form pyroxenites, which are suspected to be a major source of OIB melts (e.g. Cordery *et al*., 1997; Sobolev *et al*., 2005; Ballmer *et al*., 2013). Considering the various interactions between melts and mantle reservoirs at a relatively crude scale, this model does not account for the large diversity in terms of composition or the geochemical signature of lavas observed among the various Hawaiian volcanoes (e.g. Frey & Rhodes, 1993; Bianco *et al.*, 2008).

Following the detailed studies of Frey & Clague (1983) and Clague (1987), all studies that focused on the geological, petrographical, mineralogical, geochemical and isotopic features of Hawaiian magmatic rocks agree that the Hawaiian volcanoes are affected by four magmatic stages (see Clague & Sherrod (2014) for a synthesis): (i) a preshield stage, characterized mainly by non-feldspathoidal silica-undersaturated to saturated alkaline magmas as well as tholeiite-transitional magmas; (ii) a shield stage having eruptions of volumetrically large, dominant silica-saturated tholeiitic-picritic lavas, which represent 98% of the plume-driven melts; (iii) occasionally, a postshield stage, consisting of non-feldspathoidal silica-undersaturated alkaline lavas and highly differentiated alkaline lavas; and (iv) a rejuvenated stage, comprising feldspathoidal silica-undersaturated alkaline to highly alkaline lavas. The four stages reflect variations in magma supply over time from the underlying mantle—as well as variations in the degree of partial melting of this mantle—and therefore the stages reflect variable amounts and

rates of heat supply to the lithosphere when the latter overrides the hot spot (e.g. Clague, 1987; Ribe & Christensen, 1999; Clague & Sherrod, 2014). Hofmann *et al*. (2011) developed the concept that the along-track evolution of the composition of these different types of volcanoes results from (i) the low-viscosity metasomatic melts caused by the dehydration and decarbonation of the mantle and (ii) the more viscous tholeitic melts produced by decompression and partial melting in the elongated tail of the plume driven by plate drift. Here we will illustrate that the production, percolation and local concentration of melts differ within each type of filament. Then, assuming a plume overlain by a motionless plate, we calculate the final trajectory of these concentrated melts via dykes up to their ponding in subsurface magma chambers. Finally, we show that the eventual escape to the surface of these melts greatly improve our understanding of the causes of the along-track evolution of the composition of Hawaiian volcanism. In the present study, we first discuss the link between a 2D numerical convective model of the Hawaiian plume and the trajectories of dykes that eventually cross the overriding lithosphere. Then, we study the relationship between the temperature field and the melting rate in sub-primitive mantle/ULVZ, fertilized-harzburgite and eclogite filaments. We compare this relationship with that of dry peridotite, which is assumed to represent the bulk composition of the mantle flowing inside the plume. Subsequently, we decipher how the composition of primitive melts produced in sub-primitive mantle, fertilized-harzburgite and eclogitic filaments evolves during their percolation and eventual concentration below the lithosphere. We describe how various melts mix during their respective ascents through the lithosphere and explore how these melts then evolve during their partial crystallization and eventual eruption from the various volcanoes along the Hawaiian chain. Further, we evaluate the volume of recycled sub-primitive mantle filaments required to explain the crustal volume produced along the Hawaiian chain. Finally, we combine seismic tomographic data and geochemical data to evaluate the melt compositions observed in preshield, shield, postshield

and rejuvenated-stage volcanoes of the Hawaiian chain. Specifically, our model explains the development of rejuvenated volcanism around Oahu, i.e. 300 km from Kilauea. Furthermore, we demonstrate that the elongate type of plume stem predicted by Ballmer *et al*. (2013) explains the survival of Niihau and Kaua'i rejuvenated volcanism for up to several 100 kyrs and to a distance of more than 500 km from Kilauea.

STRESS FIELD ACROSS THE LITHOSPHERE AND THE UNDERLYING ASTHENOSPHERE IN HAWAII

Magma reaching the surface from below a thick lithosphere, such in the case of the Hawaiian volcanoes, requires dykes and fractures to cross the lithosphere. The trajectories of dykes and fractures are thus closely related to the stress field of the vertical push of the lithosphere, induced by the plume at the top of the asthenosphere. Fig. 1 represents a 2D numerical model of the Hawaiian plume that uses a temperature-dependent, power-law, dry elastoplastic rheology for the mantle and where any effects due to partial melting are assumed to be negligible. More precisely, we fix the shear modulus value at 50 GPa and use the common dislocation-creep law of dry dunite determined by Chopra and Peterson (1984) to compute viscosity. The model describes the development of a plume rising from a 100 km wide hot (~1650°C) region at the base of the upper mantle (Gerbault *et al*., 2017). The top surface represents the seafloor, which is considered to be motionless. This figure presents a snapshot of the thermal, stress and effective viscosity fields a few million years after the collision of the plume with a ~100 Ma old lithosphere. Figs 1b and 1d display what we designate in the following sections as the bottom of the "lithosphere." We use the term lithosphere as designated by its rheological definition, i.e. the top zone where the mantle is weakly or not at all deformable. It represents the elastic zone, where heat is transported exclusively by conduction (~80 km thick for Hawaii), plus the highly viscous layer, where the plume flow is sluggish

297 enough to have the distribution of temperature controlled essentially by conduction. In our
298 model, the bottom of the lithosphere corresponds to a horizon where the viscosity of the mantle
299 η is ~10^{20} Pa·s, and the asthenosphere is a zone where the viscosity is slightly lower than 10^{20}
300 Pa·s. The bottom of the lithosphere lies above ~120 km (~4 GPa) and is not flat. At the plume
301 axis, the horizon attains a depth of 120 km, where the temperature is ~1200°C; along its sides,
302 however, it is about 20 km thinner and has a temperature <1100°C. Such variability at the base
303 of the lithosphere is specific to the non-linearity of rheology. This non-linearity forms a quasi-
304 motionless region between the lithosphere and the zone where the flow of the 50 km radius
305 plume rotates to the horizontal, and it causes a 1–2 order of magnitude increase in viscosity
306 across a triangular region at ~100 km depth over a distance less than ±50 km from the plume
307 axis (Fig. 1b). Below this region, the mantle flow within the plume is purely vertical within less
308 than ±25 km from its axis, resulting in a vertically oriented maximum compressive stress σ_1 to
309 the base of the lithosphere (Fig. 1a and d). In a zone within the lithosphere, at a horizontal
310 distance of less than ~40 km from the plume axis, the direction of σ_1 becomes horizontal above
311 ~80 km depth. From 70 to 50 km depth, σ_1 is completely horizontal, and it returns to the vertical
312 above 50 km (Fig. 1a and d). These superimposed horizons of horizontal compression (σ_1
313 horizontal) and extension (σ_1 vertical) result from the bending of the elastic part of the
314 lithosphere induced by the upward push of the plume. During its rotation to the horizontal, the
315 flow divides into two regimes (Fig. 1d). The flow originates from a depth of >200 km, where it
316 is vertically oriented at ~25 km from the plume axis. Thereafter, it rotates to the horizontal and
317 attains a depth of ~150 km at ~50 km from the plume axis. Finally, the flow rises along a very
318 gentle slope to reach 120 km depth at 150 km from the plume axis. In the following text, we
319 designate this flowline as the "hot border flowline" of the plume because it initially follows the
320 1500°C isotherm. Above that flowline, the intensity of the flow diminishes, as it is slowed down
321 by the motionless lithosphere. There, stress is oriented at >45° to the horizontal to become

oriented towards the direction of flow. This implies that, above the hot border flowline, dyking may drive melt upward. The flowline that moulds the border of the plume at a distance of 50 km from its axis is the cold border of the plume (Fig. 1d). The flow flattens to the horizontal at ~70 km from the plume axis and 180 km below the surface. Around that flowline, vertical velocity shows limited variability, and the horizontal velocities decrease moving away from the axis, implying that the orientation of σ_1 at this location is quasi-horizontal and that the condition is fulfilled for the development of sills rather than dykes. As we will see later, all of these conditions are important for evaluating melt trajectories within the plume.

Our model is comparable to the 3D Hawaiian plume models of Ballmer *et al.* (2011, 2013), a major difference occurring in the investigated mantle rheological laws. In Ballmer *et al.* (2011, 2013), the rheology of the mantle is dependent on temperature, pressure, composition, H_2O content and melting rate but is independent of stress and does not integrate an elastic component. Therefore, this model describes the flow and temperature only for depths >90 km, i.e. well below the elastic lithosphere, which is ~30 km thick. Finally, the 3D box models of Ballmer *et al.* (2011, 2013) are overlain by a top interface moving at the velocity of the Pacific plate (8 cm/yr) and are partially open from below and from the sides to permit the free vertical rise of the plume from the lower mantle. Given the need to access the stress field through the entire lithosphere, we concluded that only the upper-mantle plume model of Gerbault *et al.* (2017) can be used to decipher how the melts that accumulate below the lithosphere can make their way through the lithosphere and erupt at the surface. Nonetheless, many important characteristics of our model are also found in those of Ballmer *et al.* (2011, 2013); in the latter models, for example, the bottom of the lithosphere, defined as the ~10^{20} Pas high- versus low-viscosity interface, is also ~120 km deep, and the temperature and effective viscosity fields of the plumes are very similar to those of Fig. 1. However, a detailed comparison of the flow derived from our model with that of these authors shows notable differences. First, in the

Ballmer *et al.* (2011, 2013) models, the viscosity inside the top diverging portion of the plume displays a strong lateral variation of amplitude. In the 2011 model, for instance, the minimum viscosity at the core of the plume is 10^{18} Pa·s and then grades up to 3×10^{19} Pa·s at the border of the plume stem. Further, outside the plume, the viscosity steadily rises with depth—from 240 km to 420 km—where it reaches a fairly uniform amplitude of 10^{20} Pa·s, i.e., the value recovered in our model throughout the entire asthenosphere (Fig 1). Such values likely result from the lack of a stress-dependent rheology in their models; a lower viscosity due to temperature is not compensated by an increased viscosity owing to a drop in stress within low-viscosity areas (Christensen, 1984). Further, the specific lateral boundary conditions adopted by these authors drive the downstream tail of the plume parallel to but faster than plate motion; thus, the width of the plume becomes similar in dimension to the height of the convective zone (~1000 km). This effect could explain volcanic activity along the Hawaiian track and, in particular, the rejuvenated volcanism up to 500 km from Kilauea (Hofmann *et al*., 2011; Ballmer *et al.,* 2011). Seismic tomography below the Hawaiian swell confirms the presence below the lithosphere of a ~1000 km long low anomaly, oriented parallel to the plate drift, that originates at the east of the island of Hawaii (Wolfe *et al*., 2009; 2015). Such an anomaly likely includes the downflow long tails recovered in the Hofmann *et al.* (2011) and Ballmer *et al.* (2011) models. The low-velocity seismic anomaly is, however, clearly much deeper than the one displayed in these models because it reaches a wide horizon at the base of the upper mantle. It indicates that a several hundred kilometre-long hot sheet running parallel to the drift direction crosses the main upper mantle downflow of the island of Hawaii (Agius *et al*., 2017). Seismic tomography models show that such structures exist in multiple zones beneath the Pacific plate and likely represent ascending limbs of 1000 km wide rolls having axes of rotation parallel to the drift direction (French *et al*., 2013; French & Romanowicz, 2014). These observations are consistent with 3D convective models confined to the upper mantle showing that the plate drift

(i) shifts, in the upflow direction, the axis of the plumes. These plumes eventually collide with the downwelling cold limbs of polygonal convective cells; and (ii) eventually lines up the hot, buoyant plumes inside hot sheets crossing the entire upper mantle (Rabinowicz *et al*., 1990). Ballmer *et al.* (2013) introduced a denser eclogitic component to their plume model that melts above 410 km. This melting leads to the pooling of the plume inside a long horizon above this depth and eventually to a double layering of the convective flow above and below 410 km depth. It ends with the generation of ~300 km wide rolls having their axes parallel to the plate drift; these rolls are eventually superimposed by the already complex 3D-plume flow (Ballmer *et al*., 2013; Dubuffet *et al*., 2000). This result demonstrates (i) why a narrower and much faster vertical plume anchored above 410 km depth requires the relay of the deeper plume and eventually collides at 120 km depth with the bottom of the overriding lithosphere; and why (ii) the downstream tail is so long and locally flows much faster than the top plate. To explain the volume of melt of the shield volcanoes, the vertical velocity of the axis of the narrowed plume must reach ~1 m/yr compared with the ~8 cm/yr of the Pacific plate drift. Therefore, plate drift eventually plays a negligible dynamic effect at the very top of the narrowed plume and explains a posteriori the strong analogy between the top plume morphology of the Ballmer *et al*. (2013) model (size, temperature, viscosity fields) and our Fig. 1 model topped by a motionless lithosphere.

ADIABATIC TEMPERATURE FIELD INSIDE THE PLUME AND MELTING RATES IN THE ASTHENOSPHERE ABOVE 5 GPA

In this study, we assume that (1) the H_2O and CO_2 concentrations in sub-primitive/ULVZ and fertilized-harzburgite filaments are 500 ppm and 1000 ppm, respectively, in agreement with the estimate of the mantle source contents of Hawaiian lavas studied by Dixon *et al. (*1997); (2) the eclogite filaments are formed by material that was fully dehydrated during subduction (e.g.

Godard, 2001); (3) the temperature at the border of the plume follows the mantle adiabat, as determined by Katsura *et al.* (2010), which has a potential temperature at atmospheric pressure of 1360°C and a 0.45°C/km gradient above the MTZ (Fig. 2). Finally, the most controversial point concerns the temperature profile along the plume axis. Here, we adopt the same adiabatic gradient as that of the plume border (0.45°C/km), whereas the potential mantle temperature inside the plume axis is assumed to exceed the adiabatic temperature by several hundred degrees. For the consequences of the modification of those assumed values within reasonable ranges, we refer to supplementary material A1.

By using a thermometric method based on olivine-liquid equilibria (K_D(Fe-Mg)ol-liq), Putirka (2005) inferred a potential axial temperature for the Hawaiian mantle plume of 1688°C ± 50°C. More recent studies have shown that this approach is characterized by large uncertainties and, in the case of the Putirka (2005) method, could overestimate the potential mantle temperature (Herzberg *et al.*, 2007; Herzberg, 2011; Matthews *et al.*, 2016). Fig. 2 displays the dry solidus of lherzolite, as determined by Herzberg *et al.* (2010), which shows that (i) at a depth corresponding to 3 GPa, the dry solidus is ~1480°C, i.e. ~200°C lower than the lowest estimate of the axial temperature; (2) at 5 GPa the dry lherzolite solidus is ~1670°C, below the minimum axial temperature estimated by Putirka (2005) (1705°C or a potential temperature of 1640°C); and finally (3) at 8 GPa depth, the solidus crosses the maximum axial temperature at ~1850°C. As well, at 3 GPa, 5 GPa and 8 GPa, the excess temperatures with respect to the lherzolitic solidus required to reach the cpx-out threshold are 125°C, ~80°C and ~40°C, respectively. These estimates are based on Eqn. 9 and the parameter values given by Katz *et al.* (2003) and assume that cpx-out occurs at a degree of melting ~35% in agreement with the data of Jaques & Green (1980). Using these last numbers, we can deduce that at 5 GPa, the cpx-out of dry lherzolite is 1670°C + 80°C = 1750°C, a value in between the extreme values (1705°C and 1805°C) of the axial temperature of Putirka (2005) (Fig. 2). Furthermore, at greater depth, that

421 threshold notably exceeds the maximum possible temperature along the plume axis; for
422 example, at 8 GPa it is ~1850°C + 40°C = 1890°C, whereas the maximum possible axial
423 temperature is 1850°C (Fig 2). It is important to note that at 3 GPa the situation is the opposite:
424 the range of possible axial temperature (1680–1780°C) notably exceeds the estimate for cpx-
425 out (here ~1480°C + 125°C = ~1600°C). Considering that the Hawaiian plume is overlain by a
426 120 km thick (4 GPa) plate, the temperature in the plume at 3 GPa is <1200°C, implying that
427 no dry melting is possible at this depth. Between 4 GPa and 5 GPa depth, the situation is more
428 difficult to evaluate, because both in our model and that of Ballmer *et al.* (2013) the convective
429 boundary layer, separating the centre of the plume from the lithosphere, is located at these
430 depths. According to these models, however, the temperature in the boundary layer is lower
431 than 1600°C, which corresponds to the solidus of the mantle only at 4 GPa. Such an estimate
432 opens the possibility that dry melting may occur at these depths; regardless, this dry melting
433 must be quite limited. Finally, all these temperatures indicate that between 5 and 8 GPa, a
434 marked melting of dry lherzolite is only possible if one assumes an axial temperature exceeding
435 by several 10°C the lower range of that estimated by Putirka (2005), which, according to Fig.
436 2, corresponds to a potential temperature of 1640°C. These estimates show that the melting rate
437 in the plume axis below the 4 GPa thick lithosphere is very low but that, if the potential
438 temperature exceeds 1640°C by several tens of degrees, significant volumes of tholeitic or
439 picritic melts must be produced at about 5 GPa or above. This scenario contradicts the
440 petrological and geochemical analyses of the shield-stage melts of Hawaii, which show that
441 they result essentially from a partial-melting process occurring along the spinel/garnet interface,
442 i.e. at 70 km depth, and at a potential temperature of 1500°C (McKenzie & Bible, 1988;
443 McKenzie & O'Nions, 1991). Accordingly, we assume here that the potential temperature at
444 the axis of the plume follows the potential temperature of 1640°C, for which dry lherzolite

mantle melting is expected to be negligible or even impossible immediately below the lithosphere.

The presence of CO_2 decreases the solidus of lherzolite by up to 600°C (Dasgupta & Hirschmann, 2006). Further, the solidus of mantle peridotites is nearly independent of the bulk CO_2 concentrations of the mantle, provided CO_2 exceeds 5 ppm (Dasgupta & Hirschmann, 2007). It is inferred that the CO_2-rich lherzolite solidus profile lies below the adiabatic temperature through the entire sublithospheric upper mantle (Fig. 2). However, the composition of interstitial melt depends strongly on temperature. When the temperature is much lower than that of the dry mantle solidus, the composition of the interstitial melt is carbonatitic, i.e. the CO_2 concentration of the melt in equilibrium with the rock represents ~40% of the melt mass. For temperatures relatively close to that of the dry solidus, however, kimberlitic-like melts with ~10% CO_2 are produced (Dalton & Presnall, 1998). More precisely, at 5 GPa and 10 GPa, i.e. ~150 and ~300 km depth, respectively, the kimberlite-like interstitial melt forms at ~1700°C and above 1800°C, respectively (Brey *et al.*, 2009; Shatskiy *et al*., 2013). Between 5 GPa and 10 GPa, a temperature of ~1450°C is sufficient to form interstitial melts having a composition that is "intermediate between that of kimberlite and carbonatite" but containing a CO_2 concentration of ~40% (Ghosh *et al*., 2014). As the solubility of CO_2 in mantle rocks is very low (~5 ppm), the quantity of CO_2 dissolved in the melt likely represents that of the entire solid and interstitial melt volume. As stated above, assuming that the total concentration of CO_2 in a sub-primitive/ULVZ mantle or fertilized harzburgite is ~1000 ppm, we can infer that the ratio of the mass of the interstitial melt to that of the mush, which we note as ϕ_r, ranges between ~0.25% and 1% when the interstitial melt is intermediate between a carbonatite-like and a kimberlite-like melt.

The influence of H_2O on the mantle solidus is more complex. Experiments testing the mantle conditions of the MTZ show that if the rock contains 2 wt.% water, i.e. exceeding the water saturation at that depth, the wet solidus is ~200°C lower than that of the dry solidus, up to a pressure of 14 GPa (~420 km depth; Fig. 2). Given that the maximum concentration of H_2O assumed in our filaments is ~500 ppm, and thus much lower than the water solubility of the mantle in the MTZ (>2000 ppm, Bercovici & Karato, 2005), we can infer that hydrous melting is not expected inside the MTZ. Further, between 3 GPa and 8 GPa, a 150°C temperature drop of the solidus is expected for a lherzolite containing 500 ppm of H_2O (see Fig. 1 from Katz *et al.*, 2003). Assuming that the excess of temperature above the solidus required to reach cpx-out remains the same for a dry and a H_2O-rich lherzolite (see above), we can also deduce that the temperature needed to reach the cpx-out threshold at 3 GPa, 5 GPa and 8 GPa for wet lherzolite is ~1500°C − 150°C + 125°C = ~1470°C, 1670°C − 150°C + 80°C = ~1600°C and ~1850°C − 150°C + 40°C = 1740°C, respectively (Fig. 2). To summarize, we therefore hypothesize that at ~5 GPa, the adiabatic temperature is ~1440°C, the wet solidus of lherzolite is ~1520°C and the cpx-out temperature is ~1600°C. Such a reasoning maintains that when the temperature is >1600°C, picritic melts are produced at 5 GPa owing to the drop of the solidus because of the presence of H_2O. However, relatively close to the axis where the temperature is slightly greater than that of the wet solidus (1520°C) but lower than 1600°C, tholeiites could be produced instead of picrites. Eventually, these tholeiites incorporate all CO_2 and H_2O from the sub-primitive/ULVZ mantle filaments. When the temperature is slightly lower than 1520°C, the mantle no longer melts, and the interstitial carbonate-rich melt keeps its initial mass fraction, ϕ_r = 0.25%. It is striking to note that because of the H_2O concentration of the sub-primitive/ULVZ mantle, the temperature at which the interstitial melt is kimberlite-like is greater than 1600°C and 1700°C at 5 GPa and 10 GPa, respectively (Brey *et al.*, 2009). We therefore propose that through a 100°C interval centred on the plume axis, the interstitial melt is kimberlite-like and

493 the mass fraction is $\phi_r = 1\%$. Away from this interval, however, the interstitial melt has a greater
494 CO_2 concentration and, thus, ϕ_r decreases down to the border of the plume where $\phi_r = \sim 0.25\%$.
495 These results are important because they demonstrate that at ~5 GPa, a tube of flow, having a
496 significant radius compared with that of the plume (~25 km according to Fig. 1d), can produce
497 tholeiite-picrite melts.

498 The above-mentioned estimates depend highly on pressure (and therefore depth); at 4 GPa for
499 instance, the dry solidus occurs at 1600°C, thereby suggesting that even a dry lherzolitic mantle
500 could partially melt along the plume axis. Conversely, the dry solidus reaches 1720°C at 6 GPa,
501 and from the above reasoning, we can hypothesize that even dry partial melting at that depth
502 can occur. We must also mention that the Herzberg *et al.* (2010) dry solidus profile produces
503 higher temperatures than other estimates; at 5 GPa; for instance, the dry solidus occurs at
504 1670°C, 1650°C and 1630°C for Herzberg *et al.* (2010), Hirschmann (2000) and Katz *et al.*
505 (2003), respectively. This drop of the estimated dry solidus implies that the window for wet
506 partial melting simply drifts down to 6 GPa when the Hirschmann (2000) or the Katz *et al.*
507 (2003) solidus is assumed.

508 An important question does arise from the above reasoning: Does fertilized harzburgite have
509 the same melting behaviour as lherzolite? Unfortunately, we cannot use the studies of Katz *et*
510 *al.* (2003) and Ballmer *et al.* (2013) to answer this question, as they did not explicitly consider
511 the case of harzburgitic mantle. Maaloe (2004) performed laboratory experiments at pressures
512 <3.5 GPa and demonstrated that the dry solidus of mantle harzburgite clearly lies 150°C above
513 that of dry lherzolite, i.e. at ~1670°C + 150°C = 1820°C and ~1850°C + 150°C = 2000°C at 5
514 GPa and 8 GPa, respectively (Fig. 2). Moreover, it has been observed that immediately above
515 the solidus, melts having a tholeiitic composition can be produced (Maaloe, 2004; Herzberg &
516 Asimow, 2015). If we assume, such as for lherzolite, that a 150°C drop of the hydrated solidus

occurs when the H_2O concentration is 500 ppm, i.e. it coincides approximately with the dry lherzolite solidus, we can deduce that the hydrated solidus for fertilized harzburgite may be ~1670°C and ~1850°C at 5 GPa and 8 GPa, respectively, i.e. about 80°C below and just equal to the maximum temperature of the plume at 5 GPa and 8 GPa, respectively (Fig. 2). It remains that inside the Hawaiian mantle plume stem, the partial melting of fertilized-harzburgite filaments depends essentially on the CO_2 concentration. Unfortunately, there have been no laboratory experiments in which materials resembling hydrated and carbonated fertilized harzburgites have been partially melted. We only know that between 5 GPa and 10 GPa, the melting temperature of sodium carbonate (Na_2CO_3) increases from ~1400°C to 1520°C, whereas that of calcium carbonate ($CaCO_3$) fluctuates around 1720°C (Li *et al*., 2017). As the fertilization of harzburgite implies an enrichment in alkali and other trace elements such as the light rare earth elements (LREEs), we deduce that the partial melting of such filaments must follow approximately the melting temperature of Na_2CO_3; thus between 5 GPa to 10 GPa, carbon-rich interstitial melts are produced, regardless of their position within the plume. As well, because the temperature along the plume axis is close to that of the harzburgite hydrated solidus, kimberlite-like melts may be produced, whereas to the sides of the axis, the melts should be carbonatite-like.

Finally, we must consider the melting temperature of the recycled eclogite. Given the dehydration of eclogite during subduction, the recycled eclogite is likely dry (Dixon *et al*., 2002). As well, at 5 GPa the dry solidus versus liquidus interval of eclogite and residual eclogite is at 1400°C and 1550°C, respectively (Rosenthal *et al*., 2014; Fig. 2). These temperatures imply that for a large fraction of the plume section, the dry eclogite melts completely along the plume axis and partially melts along its border (Fig. 2).

FATE OF THOLEIITE-PICRITE MELTS OF SUB-PRIMITIVE/ULVZ MANTLE FILAMENTS FLOWING INSIDE THE HOT CENTRE OF THE PLUME

There is now a good understanding of the physics of melt-rock separation during partial melting. The explicit incorporation of these processes into mantle plume models is, nonetheless, impossible because it requires grid sizes that are two or three orders of magnitude smaller than those required for modelling mantle convection. Studies of the transition zone between the mantle peridotites and the gabbroic crust in the Oman ophiolites have revealed multiple consequences of what can occur when ~20% of interstitial tholeiitic melt is produced below an oceanic ridge (Rabinowicz *et al*., 1987; Ceuleneer & Rabinowicz, 1992; Rabinowicz & Ceuleneer, 2005). This initially consolidated mantle mush, overlain by a gabbro horizon, rapidly separates into two phases: one phase composed of a melt having few crystals (near zero to 10%) and a viscosity similar to that of pure melt; the other phase is a consolidated rock having an interstitial melt concentration buffered at 5% (Rabinowicz *et al*., 2001; Rabinowicz & Toplis, 2009). The transient, interstitial upward percolation of tholeiitic melt dissolves the opx of the surrounding mantle to form restites having a dunite composition (Ceuleener & Rabinowicz, 1992). This is evidenced by the presence, in the same dunitic layer, of relics of troctolitic horizons—up to 10 m thick—illustrating the transient concentration of the tholeiitic melt inside compaction waves; the melt eventually intrudes as dykes within the overlying gabbro horizon (Rabinowicz & Ceuleneer, 2005).

Is it possible to have a situation similar to that observed in ophiolites during the partial melting via decompression of sub-primitive/ULVZ mantle filaments, between 4 and 5 GPa and at >1550°C, leading to tholeiite-picrite melts representing up to 35% of the mass of the mush? Numerical modelling–based studies have led to the concept that, during compaction, interstitial melt within the mantle may be collected within very narrow and raised vertical tubes (Connolly

564 & Podladchikov, 1998; Connolly & Podladchikov, 2007; Räss *et al*., 2019). One of these
565 models is presented in Fig. 3a. The model requires two ingredients: (1) a mantle mush where
566 the initial melt concentration drops above a given depth and (2) a mush viscosity that drops by
567 a few to several orders of magnitude when the melt pressure p_f of the mush is greater than that
568 of the solid p_s. The former condition represents an obstruction to the upward percolation of melt
569 because of the drop in permeability owing to a decrease in interstitial melt, whereas the latter
570 corresponds to a decompaction viscosity drop due to the solid grains that form the mush being
571 weakly stuck together and therefore implying that the mush is close to its deconsolidation
572 threshold. Therefore, it is easier to separate the grains using the excess pressure p_e ($p_e = p_f - p_s$)
573 than to deform the grains plastically to permit the upward percolation of melt (Connolly &
574 Podladchikov, 2007).

575 Connolly & Podladchikov (1998) investigated this hydrodynamic situation more than 20 years
576 ago; however, there are no convincing natural cases to which this description of melt
577 percolation in the mantle can be applied. This lack of application relates to upward obstruction
578 being generally ascribed to a horizon where the mush permeability is low, whereas a marked
579 drop in viscosity because of decompaction is generally associated with a high permeability
580 horizon. We argue, however, that this situation can occur when tholeiites-picrites are produced
581 within a mantle plume at 5 GPa. First, the upward obstruction to melt percolation cannot be
582 attributed to a drop of upward melt concentration. A single order of magnitude drop in viscosity
583 of the mush occurs when the interstitial melt concentration within the mantle exceeds ~5%
584 (Hirth & Kohlstedt, 1995). According to our model, this situation must occur inside filaments
585 located close to the plume axis at a pressure somewhere above 6 GPa (see above). Such a
586 viscosity drop increases the upward ductile velocity inside the filament and, consequently,
587 locally reduces the thickness of the filament and generates compressive horizontal stresses σ_1
588 (see Fig. 3b). In return, the compression leads to a horizontal coalescence of the grains that

589 compose the mush and, thus, a marked reduction of the vertical permeability of the mush
590 without implying a macroscopic reduction of the bulk melt concentration of the mush
591 (Rabinowicz & Toplis, 2009). This reasoning explains the local development of an obstruction
592 inside the plume at ~6 GPa depth (Fig. 3b). Then, because of the accumulation of melt below
593 the zone of reduced filament thickness—arising because of the later obstruction and increased
594 melting rate owing to decompression—the interstitial fluid progressively wraps a greater
595 surface of the grain boundaries within the mush. This process leads to a progressive reduction
596 of the cohesion of the mush, which can eventually be reduced to zero when the local melt
597 concentration surpasses the deconsolidation threshold in the mush, at a degree of melting of
598 ~30%, i.e., at a melt fraction of lherzolites where the interstitial melt has a picrite composition
599 (Rabinowicz & Toplis, 2009). When the excess pressure p_e exceeds the stress required to
600 separate the grains, the mush is then fully deconsolidated. The implication is that its viscosity
601 becomes that of a suspension, i.e., dramatically lower than that of the bottom of the compaction
602 wave, where p_e is negative and the mush continues to behave as a consolidated medium. As a
603 result, inside the core of the wet filaments, the selected conditions required to generate vertical
604 melt tubes are fulfilled, providing an efficacious way for the melt to propagate up to the base
605 of the lithosphere (Fig. 3a). An important question concerns the estimation of the tube thickness
606 δ. According to Connolly & Podladchikov (2007), δ is $\sim L\sqrt{\mathrm{R}}$, where L represents the
607 compaction length defined by Eqn. 2 (supplementary material Table S1) , and R represents the
608 amplitude drop of the solid viscosity during decompaction, i.e., when the local melt
609 concentration reaches ~30% over that at the initiation of the obstruction (i.e. ~5%). According
610 to Rabinowicz and Ceuleneur (2005), L is on the order of kilometres. Further, the R factor may
611 be extremely small, in the order of 10^{-6}, indicating that δ can be on the scale of metres.

612 To hold back this melt along the bottom of the lithosphere, the effective pressure p_e at the top
613 of the tubes must be lower than the fracturing limit of the lithosphere, which is ~50–100 MPa

614 (Grégoire *et al*., 2006). Because of the low viscosity of the melt, the excess pressure p_e drop
615 due to the melt flow in tubes is negligible. Therefore, p_e at the top of the tubes approximates
616 that of the buoyancy of the melt integrated along the total height H of the tubes (here ~30 km,
617 i.e. the distance separating the base of the lithosphere from the zone of production of picrites at
618 5 GPa):

619 $$p_e = \delta\rho g H = \sim 150\ MPa, \qquad \text{(Equ. 1)}$$

620 where g is the gravity constant, and $\delta\rho$ is the solid-melt density contrast (~500 kg/m^3). This last
621 value is consistent with estimates of densities of carbonatitic to hydrous silicate melts, which
622 range from 2600 kg/m^3 to 3000 kg/m^3 at 5 GPa (Dobson *et al.*,1996; Spera,1984 and Matsukage
623 *et al.*, 2005), and a mantle density at this depth of ~3420 kg/m^3 (Kaban *et al.*, 2016).
624 Consequently, with these parameters, upon the height of the tubes reaching a value H_{dyke} less
625 than ~20 km, the vertical dykes arise in the mantle, and the melt drains through these dykes.
626 The dyke thickness, depending on both the elastic parameters and the amplitude of excess
627 pressure, is on the scale of metres (i.e. Grégoire *et al.*, 2006). After penetrating the lithosphere,
628 the dykes follow the trajectory of σ_1, which is oriented vertically above the plume at the bottom
629 of the lithosphere (Figs. 1 and 3c). When σ_1 is not perfectly vertical, the excess pressure p_e at
630 the top of the dyke tends to drop. Accordingly, dyke thickness decreases. To maintain the total
631 melt volume transported by the dykes, however, the heights of the dykes increase and eventually
632 preserve an excess pressure at their tops, buffered to the critical threshold for fracturing. Such
633 a process allows the upward free movement of dykes. Being metres in thickness, dykes not only
634 transport melt but also solid crystals and xenoliths. Finally, when the apices of the dykes rise
635 above 70 km, where σ_1 rotates to the horizontal (Figs. 1 and 3c), they transform into sills of
636 several tens of kilometres in length and probably a few metres in thickness (Maccaferri *et al*.,

637 2011). The superposition of these sills, likely set between 70 and 50 km depth, produces a
638 laterally extensive magma chamber, which we label the "shield magma reservoir".

639 Before melt intrusion into the shield magma reservoir, a dry mantle horizon at this depth is
640 characterized by temperatures between 600°C and 750°C, and an effective viscosity of ~10^{23}
641 Pa·s (Fig. 1). Moreover, the ponded tholeiite and picrite melts are highly reactive because they
642 contain 0.3% CO_2 and 0.15% H_2O since they comprise up to 30% partial melt of a mantle
643 containing 1000 ppm and 500 ppm of CO_2 and H_2O, respectively. Thus, three mechanisms
644 contribute simultaneously to heat and eventually reduce the effective viscosity of the solid
645 fraction of the shield magmatic reservoir: (1) heating of the mantle at the contact of the sills;
646 (2) partial crystallization of the ponded melts during cooling; and (3) diffusion of the volatiles
647 from the melt into the surrounding mantle. Eventually, these processes reduce, by a few orders
648 of magnitude, the effective mantle viscosity of the shield magmatic reservoir. As the reservoir
649 is relatively thick (~20 km), its timescale of thermal relaxation are long (>10 Ma). If we assume
650 that the effective viscosity of the lithosphere, where the shield magmatic reservoir becomes
651 established, is 10^{20} Pa·s (instead of 10^{23} Pa·s prior to the accumulation of melt from the dykes),
652 then the compression induced by the bending of the plate in the shield magmatic reservoir,
653 having an amplitude of 30 MPa (Fig. 1) and a time-lapse of 0.1 Ma, produces a total shear ε of
654 ~10^{20} Pa·s / $3 \cdot 10^7$ Pa $\times$ $3 \cdot 10^{12}$ s = ~1. If we recall that ε = ~0.5 yields a total deformation γ (the
655 ratio of the long axis of the deformation with the short axis) of ~4, we therefore expect ε= 1 to
656 produce a γ = ~16. Such deformation rates likely induce a strong folding of the sills that form
657 the reservoir (Fig. 3d). This folding provokes a marked concentration of melt at the axis of the
658 folds. At the top of these folds, vertical fractures are generated and eventually drain the ponded
659 melt of the shield magmatic reservoir (Barraud *et al*., 2004; Weinberg *et al*., 2015). Finally,
660 when the tops of the fractures reach a depth of ~50 km, where σ_1 is again vertical, vertical dykes
661 are generated, transporting melts to near the surface (Fig. 3d). Therefore, their trajectories

depend strongly on the elastic stress field induced by the volcanic structure or by the crust itself. This stress field can both curve the trajectories of dykes, which eventually pond as sills inside a subvolcanic magma chamber or cause an eruption at the surface (Pinel & Jaupart, 2003; Maccaferri *et al*., 2011; Pinel *et al*., 2017). The evolution of the composition of transported lavas depends greatly on what occurs during this last stage of the melt flow. In supplementary material A, we show that the temperature inside the 'shield reservoir" can account for the compositions of the melts erupting at the surface. Finally, the situation is similar for tholeiite-picrite melts produced in the hot diverging part of the plume, i.e. above the hot flowline (Figs 1d and 3c) but at a sufficient distance from the plume axis, i.e. greater than ~40 km, to allow dykes carrying the melts to avoid the shield magmatic reservoir. These melts are not affected by melt mixing or interactions with the mantle lithosphere occurring in and around the shield magmatic reservoir. Melt-mixing and fractional crystallization processes may eventually occur when these dykes reach a subcrustal horizon at a distance of ~100 to ~180 km from the plume axis.

FATE OF THE CARBON-RICH INTERSTITIAL MELTS OF FERTILIZED-HARZBURGITE FILAMENTS FLOWING INSIDE THE HOT CENTRE OF THE PLUME

The above-mentioned migration processes are specific to sub-primitive/ULVZ mantle filaments flowing close to the plume axis. In this section, we concentrate on the possible mobilization, inside the plume at 5 GPa of CO_2-H_2O-rich melts produced within fertilized-harzburgite filaments. Here, the temperatures of the solidus and the cpx-out of the 500 ppm-rich fertilized hazburgite are 1670° and 1760°C, respectively, whereas the axial temperature is 1710°C (see above). It is inferred that the melting rate, even along the axis of the plume itself, remains small at 5 GPa depth in the fertilized hazburgite (Fig. 2). Accordingly, the rheological softening

686 expected when the interstitial melt concentration surpasses 5% does not occur. Thus, one of the
687 conditions required to generate narrow vertical tubes is not fulfilled. Because of the severe
688 obstruction of the upward percolation of melt located at the bottom of the lithosphere, i.e. below
689 4 GPa, however, compaction waves are generated. This process agglomerates melts within
690 separate pockets having thicknesses of ~2 × L (Rabinowicz & Ceuleneer, 2005; and Fig. 4a).
691 Here, L designates the compaction length (Eqn. 2):

692 $$L = \sqrt{\frac{k(\phi_0)\eta}{\phi_0 \mu}}, \qquad \text{(Equ. 2)}$$

693 where η and μ represent the viscosity of the solid fraction of the mush and the melt, respectively.
694 $k(\phi_0)$ is the permeability of the mush evaluated at ϕ_0, the initial volume of the interstitial melt
695 ($\phi_0 = 1.2\phi_r$, with ϕ_r ranging between 0.25 and 1% when the interstitial melt is intermediate
696 between carbonatitic-like and kimberlite-like melts; see above). A good approximation of $k(\phi_0)$
697 is given by Wark & Watson (1998):

698 $$k(\phi_0) \approx \frac{a^2 \phi_0^3}{200}, \qquad \text{(Equ. 3)}$$

699 where a is the solid-grain size (here ~3 mm). From Eqn. 3, we can derive $k(1.2\%) = 10^{-13}$ m^2
700 and $k(0.3\%) = 1.6.10^{-15}$ m^2. As well, the viscosity of a hydrated kimberlite melt μ at 1700°C
701 and a depth of 5.5 GPa is ~0.5 Pa·s (Persikov *et al*., 2017), whereas the viscosity at a similar
702 depth and temperature for a carbonatite melt is slightly less than 10^{-2} Pa·s (Kono *et al*., 2014).
703 Considering that η, the effective viscosity of a hydrated lherzolite mantle, is about ~10^{19} Pa·s,
704 i.e. a value consistent with the 10^{20} Pa·s value observed below the lithosphere in our dry mantle
705 plume model (Fig 1) combined with an order of magnitude extra drop linked to the water
706 content of the filament (Karato & Wu, 1993), then L = ~15 km for both values of the mass of

melt to bulk rock ratio ϕ_r and the viscosity of the kimberlite-like or carbonatite-like interstitial melt μ.

Fig. 4a presents a 1D snapshot of the distribution of melts after a period of $15 \times \frac{L}{v_{int}} =$ 80 ka, where v_{int} is the interstitial melt velocity, as derived from Darcy's law (Eqn. 4):

$$v_{int} = \frac{\delta \rho g k(\phi)}{\mu_\phi} = \sim 2.5 \text{ m/yr.} \qquad \text{(Equ. 4)}$$

Over 80 kyr, the interstitial melt percolates upward by ~200 km. The melt accumulates below the base of the lithosphere, i.e. at a depth of ~120 km (pressure of ~4 GPa; see above). This accumulation initiates a first uppermost compaction wave, $2 \times L \approx 30$ km thick, below 120 km, followed by subsequent waves situated 60 km below each other (Fig. 4a). The upward percolating melt accumulates initially on the highest wave. Between two successive waves, the melt concentration decreases progressively, and thus the Darcy velocity here becomes quasi-zero. Finally, after 80 kyr, the amplitude of the uppermost wave approaches $\sim 10 \times \phi_r$. It is important to note that all values adopted in our model are consistent with those used by Hofmann *et al*. (2011). The main difference between the two models is that Hofmann *et al*. only studied the Darcy percolation of the interstitial melt; they did not include the simultaneous formation of compaction waves.

Assuming that the vertical distribution of the melt in waves is sinusoidal, we can estimate that the mean concentration of melt inside the top wave is $\sim 2 \times \left(\frac{10}{\pi}\right)\phi_r = \sim 7 \times \phi_r$. It is inferred that the mean concentration of H_2O in the mush is ~7 × 500 ppm = 0.35 wt.%, i.e. H_2O represents ~0.35% of the mass of the mush. Similarly, the CO_2 concentration is ~0.7 wt.%. Considering the above estimate of the dry solidus of harzburgite at 1820°C and the liquidus of olivine, which is the most refractory mineral of peridotites, at 1950°C (Herzberg & Asimow, 2015), we

propose that the gap between the dry solidus and the liquidus of the harzburgitic mantle at 5 GPa defines a very narrow range from 1820°C to 1950°C. As proposed by Katz *et al.* (2003) for lherzolites, we assume that the solidus versus liquidus interval of a mantle harzburgite containing 0.3 wt.% of H_2O is reduced by 500°C compared with that of a dry harzburgite. We therefore deduce that at 5 GPa, the solidus versus liquidus interval of a harzburgite containing ~0.3 wt.% (3000 ppm) H_2O ranges between 1320°C and 1450°C. The latter value is very close to the adiabatic temperature of the mantle at 5 GPa (1440°C, Fig. 2). Therefore, the presence of the ~7 × ϕ_r of kimberlitic or carbonatitic interstitial melt inside the top compaction wave leads to the complete melting of the solid fraction of the mantle within the wave. The composition of the produced melt is a mix of 7% kimberlite-like or 1.8% carbonatite-like melt and the remaining melt being molten fertilized harzburgite. These melts have similar major element compositions as those of meimechites from the Siberian large igneous province (Table S2A). Our proposition also agrees with Panina & Motorina (2013), who studied melt inclusions occurring in olivine phenocrystals from meimechite lavas and associated cumulative dunites. They determined that these melt inclusions represented a meimechite melt produced by a high degree of partial melting of a mantle source. Accordingly, for the following discussion, we use the term “meimechite-like” melts. As a consequence of the complete melting of the harzburgite along the plume axis in the uppermost compaction wave, a 30 km thick layer of pure melt accumulates below the lithosphere, here at ~120 km depth (Fig. 4b). It also imposes an excess pressure p_e of 0.15 GPa at the base of the lithosphere, which ends with the generation of meimechite-like dykes having the same trajectory as the tholeiite-picrite dykes generated above the sub-primitive/ULVZ mantle filaments. In particular, when the dykes eventually pond in the shield magmatic reservoir, the folding of the sills must cause the meimechite-like and tholeiite-picrite melts to mix. Finally, in supplementary material A, we discuss melt segregation when

753 meimechite-like dykes avoiding the shield reservoir pond in sub-crustal magma chambers
754 below pre-shield and post-shield volcanoes.

755 TRAJECTORY OF MELT PRODUCED IN FERTILIZED-HARBURGITE AND SUB-
756 PRIMITIVE MANTLE/ULVZ FILAMENTS ALONG THE PLUME BORDER

757 Determining the upward percolation of volatile-rich melts close to the border of the plume is
758 more complex because this vertical movement also depends on trajectories of the ductile flow
759 within the plume, which are not purely vertical. A first consequence is that filaments tend to
760 become more horizontal. This is clearly the case for filaments that follow the cold border
761 flowline and become more horizontal at a distance of ~70 km from the plume axis and at a
762 depth >180 km (~6 GPa; Figs. 1d and 4b). Hence, the upper interface of each filament
763 corresponds to a zone composed of dry peridotite, which does not partially melt and thus has a
764 zero permeability, i.e. it fulfils the condition for concentrating the carbonatitic interstitial melt
765 in compaction waves in the underlying vertically oriented fertilized-harzburgite or sub-
766 primitive mantle filaments that form because the local temperature is close to the mantle
767 adiabatic temperature, i.e. ~1410°C, a value lower than the 500 ppm H_2O-hydrated solidus of
768 lherzolite at 6 GPa (~1600°C) and thus also of harzburgite (~1750°C). It is inferred that at the
769 entrance of the elbow formed during the fast rotation of the flow line to the horizontal at the
770 plume border, at a depth corresponding to 6 GPa, there is an accumulation of interstitial
771 carbonatitic melt that had previously dissolved the 500 ppm of H_2O initially present in the bulk
772 of the filament. This melt is reactive with both the filament and the surrounding dry peridotite
773 and thus contributes to metasomatizing them. Accordingly, mafic silicate melt can form and
774 mix with the carbonatitic interstitial melt to produce kimberlite-like melts. In the present
775 situation, the interstitial melt cannot escape upward via dykes because of the horizontally
776 oriented σ_1, in contrast with flowlines inside the plume core where σ_1 is vertically oriented. (see

Fig.1). Beyond the entrance of the horizontalized section of the elbow, the compaction leads to accumulation of volatile-rich melt along the top of the filament. At a distance of 75 km from the plume axis, the cold flowline has a 10°–20° slope leading to a horizontal upper limit at about 140 km depth, i.e. ~10 km less than the depth corresponding to 5 GPa and at a distance of 175 to 250 km from the plume axis (Fig. 4b). Melt percolation experiments inside a sloped partially molten layer show that (1) compaction pockets migrate upward and accumulate at the apex of the layer and (2) the pressure excess p_e there reflects the buoyancy of the melt integrated from the bottom to the top of the inclined layer (here ~40 km, between 180 and 140 km depth). This value represents a pressure excess p_e of 0.2 GPa, a value exceeding the threshold limit for fracturing by a factor of ~2 (Rabinowicz & Ceuleneer, 2005; Grégoire *et al*., 2006). Finally, because of the ascent of the cold flowline, the cold convective boundary of the plume is somewhat pinched at a distance of ~150 to 200 km from the plume axis, suggesting that trajectories of σ_1 along that boundary are vertically oriented (Figs. 1d and 4b). At the top of the sloped filaments, therefore, there is the possibility for the kimberlitic-like interstitial melts to discharge via dykes, which eventually reach the subcrustal horizon.

PARTIAL MELTING OF ECLOGITE FILAMENTS INSIDE THE PLUME

A complex question remains: What is the topology of the distribution of eclogite material inside the plume? Considering that eclogite filaments after one convective cycle are relatively thin (~500 m; see Introduction) and that eclogite has a stiff rheology relative to that of the surrounding recycled hydrated mantle, a deformation γ of ~10 for the plume during its ascent through the upper mantle (Farnetani *et al*., 2002) likely leads to boudinage of the recycled eclogitic filaments (Ramberg, 1955). Consequently, the resulting bodies of eclogite must be less than a few kilometres in height. When they melt, the excess pressure p_e at their apex is therefore likely too low (<10 MPa, Eqn. 1) to fracture the mantle located above. It is very likely

that close to the plume axis, the eclogitic melt mixes with the tholeiite-picrite melts, which accumulate within tubes that develop inside sub-primitive/ULVZ mantle filaments. Further, melt derived from eclogite filaments may also mix inside the 30 km high meimechite-like melt horizon, which develops below the lithosphere, or with the kimberlite-like interstitial melt along the cold border flowline or the plume. Occasionally, the eclogitic filament can connect over a vertical distance of several tens of kilometres. Accordingly, dykes transporting the derived melt could end either in the shield magmatic reservoir, where it mixes with tholeiite-picrite and meimechilte-like melts, or, if the eclogitic filament follows the cold flowline of the plume, it mixes with carbonatite or kimberlite melts. The presence of CO_2 and H_2O inside the resulting hybrid melts allows them to be eruptable and eventually reach the surface. This process agrees with Sobolev *et al.* (2009) who demonstrated in a melt-inclusion study that meimechite melts from the Siberian platform are volatile-rich at great depths (200–270 km; CO_2: 6 wt.%; H_2O: 2 wt.%). When the residual partially molten eclogite filaments pond at ~150 km depth and at ~200 km from the plume axis, they likely partially melt, and the surrounding kimberlitic-like dykes likely host both eclogitic melts and eclogitic xenoliths. We note that meimechite melts have not been found as melt inclusions in Hawaiian tholeiitic picrites; the presence of meimechite melts is a prediction of our model that remains to be verified by further petrological studies of Hawaiian lavas and associated olivine-rich cumulates and dunites.

ABUNDANCE OF RECYCLED FILAMENTS REQUIRED TO EXPLAIN THE VOLUME OF MELT PRODUCED IN THE HAWAIIAN CHAIN

According to the model from Fig. 1, we assume that the mantle plume below Hawaii has a radius of 50 km with an axial upward velocity of 1 m/yr. These estimates are consistent with a 1 cm/yr velocity of a 500 km radius plume in the lower mantle, which eventually transforms into a plume having a 1 m/yr velocity and a 50 km radius once it reaches the upper mantle. The

825 solid flux in the plume is therefore $2\pi VR^2/3 = \sim 5$ km^3/yr (to obtain this last equation, we assume
826 that the velocity is parabolic within the tube of radius R). The actual volume of crust produced
827 by the Hawaiian plume activity, as estimated using gravimetric data, is ~0.2 km^3/yr (van Arc &
828 Lin, 2004). Considering that tholeiite-picrite melts result from a degree of partial melting of up
829 to 30%, we find that 0.6 km^3/yr of mantle is partially molten to account for the present partial
830 melt productivity of the Hawaiian plume. Such melt is produced inside a flow tube, which at 5
831 GPa depth is delimited by the 1550°C isotherm up to the plume axis where the temperature is
832 1700°C. When the 50 km radius plume cools, it imposes, along its border, the adiabatic
833 temperature of 1440°C. Therefore, it can be shown that during the time needed for the mantle
834 located within the plume to move up from the bottom of the MTZ to near the top of the upper
835 mantle (~600 km), a temperature of 1550°C is attained at a distance less than 4 km from the
836 border of the plume, i.e. 45 km from the plume axis at depth (see Fig. 1). Therefore, ~80% of
837 the flux of the plume could provide the necessary conditions for the production of tholeiite-
838 picrite melts. If the plume was composed entirely of sub-primitive/ULVZ mantle filaments,
839 then 4 km^3/yr of mantle should have produced the tholeiite-picrite melt. As only 0.6 km^3/yr of
840 mantle is needed to explain Hawaiian volcanism, we can deduce that the sub-primitive/ULVZ
841 mantle filaments represent a fraction (0.6/4 = 15%) of the "effective" flux of the plume. This
842 estimate agrees with that proposed by Ballmer *et al.* (2013). Consequently, we conclude that
843 the Hawaiian plume is relatively poor in sub-primitive/ULVZ mantle. This result may explain
844 a posteriori why the seismic tomographic models of the Hawaiian plume display a bottom-to-
845 top maximum variation of amplitude of only 1% for V_P seismic velocities (Wolfe *et al*., 2011).
846 This is also consistent with Ballmer *et al*. (2013) who explained the entire seismic signal of the
847 mantle plume using only thermal anomalies. For us, this result is striking because a 1%
848 interstitial melt may potentially lead to a drastic drop in seismic velocity (up to 8%; i.e.
849 Hammond & Humphreys, 2000). We suggest that because sub-primitive/ULVZ mantle

filaments are sparse, the large-scale tomographic models, which have a resolution power for observing anomalies of a >100 km wavelength, simply do not image these filaments. The low volume of sub-primitive/ULVZ mantle filaments needed to explain the productivity of the Hawaiian plume is helpful because it indicates that the temperature field of our model is compatible with the thermodynamics of the melting process. More precisely, we have shown above that at 5 GPa, the temperature gap between the hydrated lherzolite solidus and the cpx-out curve ranges from ~1520°C to ~1600°C. This indicates that the 20% to 30% melting of the mantle material consumes an amount of energy corresponding to a temperature of less than 0.3 × 250°C = 75°C (Lange *et al*., 1994; Sleep & Warren, 2014). As the temperature at the plume axis is close to ~1700°C, we see that if the energy required to melt the rock is fully furnished by temperature, picrites are produced only very close to the plume axis. However, because the sub-primitive/ULVZ mantle filaments are sparse—representing ~15% of the plume flux—approximately 85% of the energy required to partially melt the filaments may be provided by conduction through the solid framework of the plume (e.g. Ballmer *et al*., 2013). We can infer that ~12°C of the bulk temperature drop, due to energy extraction by melting, is expected to produce picrites, a value that is negligible considering the uncertainty of all values considered in this study. Finally, because of the incorporation of H_2O and CO_2 into the produced tholeiite-picrite melts, the dry restite of the sub-primitive mantle filament has an elevated solidus, preventing remelt up to ~90 km depth even along the plume axis (Fig. 2).

According to our model, if we assume that the entire mantle flux of a plume is composed of sub-primitive mantle, the melt productivity of the plume can exceed 1.3 km^3/yr, a value comparable to that estimated for the Deccan traps, the North Atlantic volcanic province and the Kerguelen plateau (e.g. Coffin & Eldholm, 1994). Such a hypothesis is consistent with the so-called primitive mantle sources proposed for various LIPS, including the Kerguelen-Heard plateaus, the Siberian and Deccan traps, the Karoo province and the Baffin Island and West

Greenland flood basalts (e.g. Neal *et al.*, 2002; Jackson & Carlson, 2011). Recently, Garcia *et al.* (2020) provided evidence that Puhahonu, a 12.5–14.1 Ma volcano in the north-western-western portion of the Hawaiian Ridge, is the largest shield volcano on Earth. To explain its development, they considered various testable mechanisms for increasing magma production, including a more fertile source and a hotter mantle. By elimination, Garcia *et al.* (2020) concluded that only fluctuations in plume temperature can explain this anomaly. According to our model, the mantle that led to the construction of Puhahonu was simply more fertile in sub-primitive/ULVZ mantle filaments than the filaments currently transported by the Hawaiian plume. When the volume of filaments increases, a higher quantity of sensible heat is required to partially melt the filaments. Such an effect likely leads to a temperature decrease in the plume and reduced melting rate of filaments, favouring the production of tholeiitic melt—the dominant type of mantle-derived melts in the case of LIPs (e.g. Coffin & Eldhom, 1994; Ernst, 2014).

QUANTITATIVE MODEL COMPARISON WITH GEOPHYSICAL AND GEOCHEMICAL DATA FROM THE HAWAIIAN CHAIN

Geophysical data

Fig. 5a, b and c display the 140 km, 80 km and 60 km depth slices, respectively, of the Rayleigh wave tomographic model of Laske *et al.* (2011) around the Hawaiian region. The slices show that the 100 km wide island of Hawaii is contoured somewhat by a crown-shaped, low-velocity zone. The latter may result from the melt—produced inside the hot centre of the plume below the lithosphere—being squeezed out from the mantle and eventually ponding up to 100 to 150 km from the present axis of the Hawaiian plume. This process is corroborated by the Tilman *et al*. (2001) P-wave velocity structure at 65 km depth below the main island (Fig. 5d), which illustrates that Kilauea, Mauna Loa, Mauna Kea, Lahalai and Kohala are located well inside the low seismic anomaly crown. Strikingly, these volcanoes lie over P-wave local maxima; this

indicates that these major active or recently dormant Hawaiian shield volcanoes mostly drain accumulated melt from the shield magma reservoir and, consequently, are probably domains where the mush is concentrated anomalously in olivine-rich cumulates.

A 3D seismic velocity structure of the south-eastern part of the main island, above 20 km, is displayed in Fig. 6 (Park *et al.*, 2007). Below ~5 km, V_P velocities range between ~6 and 8 km/s (Fig. 6c and d). These velocities have been related to ultramafic cumulates that crystallized inside subcrustal magma reservoirs from which the volcanism derives (Park *et al.*, 2007). However, the shape of the structures suggests rather the development of 20 km wavelength diapirs composed of a high-velocity material intruding a low-velocity layer. In particular, the tops of the diapirs culminate below the volcanoes of Mauna Loa, Kilauea and Loihi. Given that the high-velocity material corresponds to ultramafic olivine-rich cumulates, we can deduce that, because of their density, the tholeiitic-picritic-meimechite melts transported within the swarms of dykes described in the previous sections pond below the crust (Maccaferri *et al.*, 2011). Thereafter, melts partially crystallize and form 20 km wide compaction pockets composed of a mush, having a basaltic interstitial melt and a solid fraction composed essentially of olivine crystals (Rabinowicz & Ceuleneer, 2005). These pockets eventually rise by diapirism to collide with and deform the Moho interface. The resulting interstitial melts, squeezed out during these collisions, explain the observed abnormally high velocity of diapirs, which are capped by relatively low-velocity gabbroic material. Another striking observation is that the set of high-velocity diapirs is concentrated mainly along two parallel vertically oriented arcs of cylinders centred around the axis of the Hawaiian plume (Fig. 6a). The first arc includes Loihi and eventually intercepts the coast of the main island at the location where the strongest seismic activity is recorded (Fig. 6a). The second arc, situated ~20 km seaward (Fig. 6a), likely represents subcrustal melt transported by existing dykes at ~100 km from the present plume axis. These dykes avoid the shield magma reservoir (Fig. 6). Currently, the pooling in a cold

environment of a high-density mantle mush immediately beneath the crust shows strong similarities with the crust/mantle transition zone beneath the ridge over the Iceland plume (Rubin, 1990, Rabinowicz *et al.*, 2012). These observations therefore provide information related to the ultimate ponding of dykes that drain mantle primitive melt extraction from any plume.

Unfortunately, Fig. 6 does not indicate from where the latter dykes originate. The depth distribution of the loci of the earthquakes below the rectangular horizons QQ' and RR' of the main island is drawn in Fig. 7a, and we can deduce four deep zones of earthquakes occurring in the south-eastern section of the island of Hawaii. One zone is very apparent and vertical down to 30 km below Kilauea (Fig. 7b). Two other zones of the same vertical profile correspond to ~50 km deep sources, one located beneath Mauna Loa and the other situated along the east coast of the island of Hawaii (Fig. 7a), where the first seismic low-velocity cylinder of Fig. 6a crosses the coast. A final zone corresponds to seismic loci rooted at 30 to 50 km below Loihi (Fig. 7c). It is noteworthy that all these loci are connected to swarms of earthquakes rooting at ~50 km beneath the eastern limit of the main island (Klein, 1982; Wright & Klein, 2006). Previously, we stated that the ponding of sills within the shield magma reservoir leads to the relaxation of the elastic stresses inside this domain and that the melt stored in the axis of the horizontally folded sills eventually escapes above 50 km via vertically oriented dykes (Fig. 3). Fig. 7b and c suggest that these dykes follow a path through the lithosphere created when the shield volcanoes were initiated during their preshield period (Wright & Klein, 2006). The persistence of the original preshield path of the melt through the entire lithosphere for such a long period (>1 Ma) is surprising. We speculate that, because of the persistence of the orthogonality of the σ_3-direction in the lithosphere of the Hawaiian track, it is likely that the fault plane created during the preshield stage remains largely open to drive the rejuvenated volcanism to the same shield volcano (Solomon & Sleep, 1975). For instance, the oldest ages

of Kilauea vary between 0.6 and 1 Ma, whereas the rejuvenated stage for West Maui and East Molokai began ~0.6 My ago (Garcia *et al*., 2016; Fig. 8). These three volcanoes lie along the Kea line with the two latter volcanoes located ~200 to 250 km downflow from Kilauea (Bianco *et al*., 2005). The rejuvenated stage for West Maui and East Molokai may be related to melt transport via deep open faults following the same cold flowline (Fig. 4b) at a ~200 km distance from the plume axis.

Fig. 8 displays the Watts & ten Brink (1989) estimate of the evolution of the thickness of the volcanic load and the depth of the Moho along the Hawaiian volcanic chain (Loihi volcano used as the reference point). Between Hawaii and Molokai, located at a distance of ~200 km from the plume axis, both parameters are negatively correlated. The decrease of the thickness of the load with volcanic age is consistent with the erosion of volcanoes, whereas the increase in the depth of the Moho is indicative of an underplating process related to ultramafic cumulates that crystallized within subcrustal magma reservoirs, similar to that occurring along the east coast of Hawaii (Fig. 6b). However, the negative correlation between both profiles ends between Molokai and Oahu (Fig. 8). There, the Moho depth decreases, whereas the thickness of the volcanic load continues to decrease. The decrease of volcanic load coupled with the decrease of the Moho depth is indicative of a reduction of the effective topographical weight applied to the top of the 25 km thick elastic Hawaiian plate—Watts & ten Brink (1989) explained this layer as representing the horizon where the elastic bending permanently sustains the loading induced by the various volcanic charges. The resulting elastic stress is compressive above ~12.5 km and extensional below. If we consider the horizontal tension induced at the surface of the plate by the plume, its intensity also decreases with distance from the plume axis and partly balances the elastic compressive stress generated by the volcanic loading above ~12.5 km, i.e. at crustal levels. The pressure of the volcanic load generally exceeds the vertical dynamic stresses induced by the plume; below the main island, the pressure is ~100 Mpa, whereas that

of the plume is ~30 Mpa, i.e. the magnitude of the vertical push of the ~1 km high and 1200 km wide swell surrounding the main island. The elevation of the coral reef deposits of the central Hawaiian islands, i.e. occurring around Oahu, Molokai and Lanai, is an indication that the volcanic load at ~200 km from the main island becomes negative, i.e. the elastic deflection due to the loading is reversed because of the uplift of the volcanic structure (Grigg & Jones, 1997). Above 12.5 km, the elastic stress due to the loading is, therefore, extensional rather than compressive and thus reinforces the extension induced by the plume (Watts & ten Brink, 1989; Bianco *et al*., 2005). We can infer that here, the melt that accumulates below the crust is free to erupt at the surface and, therefore, this stress reversal is the likely cause of the deep origin of the rejuvenated volcanism, which is generally marked by the eruption of kimberlite-like melt dykes commonly transporting upper-mantle xenoliths to the surface (~110–150 km; Keshav *et al*., 2007, and also see above). These details are specific to rejuvenated volcanism, implying that it constitutes the only case where mantle melts may directly erupt at the surface without differentiation in a magma chamber located either immediately below the crust (preshield/postshield and most shield magmas) and in the shield magma reservoir (lavas of the shield reservoir erupting directly at the surface). Bianco *et al.* (2005) suggest that the rejuvenated volcanism at North-Arch, Niihau and Kauai, which are also downflow volcanic structures but located quite far (up to 500 km) from the present axis of the Hawaiian plume, can be interpreted similarly. This supposes that the upward push of the Hawaiian plume is asymmetric and reaches ~500 km at a downflow distance from Kilauea. As stated in the Introduction, such an effect is not taken into consideration in our model, as it is in Balmer *et al.* (2011) and Hofmann *et al.* (2011). Accordingly, we suggest that the downflow plume proposed by these authors may lead to trajectories of kimberlite-like melt dykes initiated beneath the cold flowlines at a downflow distance of up to 500 km from the axis of the Hawaiian plume and therefore eventually explains the rejuvenated volcanism of North-Arch, Niihau and Kauai.

Geochemical features of Hawaiian magmatic rocks

Characterization of the primary melt interaction with the overlying mantle and lithosphere

*Shield volcanism***.** The shield stage corresponds to the by far most voluminous magmatic activity of the Hawaiian plume. According to our model, the shield-stage parental melts—including the high-SiO_2 tholeiites, volumetrically the most abundant during that stage (Rhodes, 2016), are produced between 5 and 4 GPa (150–120 km depth) and then pond in the shield reservoir located at about 70 km depth (about 2.5 GPa), i.e. within the spinel peridotite stability field of the Hawaiian lithospheric mantle. We therefore propose that the reaction proposed by Rhodes (2016) between melts produced within the garnet peridotite stability field and the harzburgite residues occurs in the shield magmatic reservoir within the lithosphere. The lithospheric harzburgite residues proposed by Rhodes (2016) correspond, in that case, to the dry peridotite component of our model, a component consisting mostly of lherzolites and harzburgites. We finally propose that the shield magmatic reservoir, located within the mostly anhydrous spinel-bearing lithospheric mantle and where the shield-building stage parental melts pond, corresponds to a zone of more or less intense reactions (e.g. assimilation, local melting) between those melts and the surrounding lithospheric mantle. These reactions lead to variations in major elements (e.g. SiO_2, CaO, TiO_2), isotopic ratios (e.g. Sr, Nd, Pb) and trace element ratios (e.g. Zr/Nb, Zr/Y, La/Nb) observed in shield lavas occurring at the surface of the Hawaiian archipelago. Indeed, we propose that the mantle lithosphere beneath Hawaii, which is 120 km thick at the axis of the plume, is heterogeneous, consisting of a "puzzle" composed in particular of 1) anhydrous peridotite components, including the mantle source of MORB, and 2) Loa and Kea components accreted in the lithosphere during its 90 My subsidence (Fig. 9). Harrison & Weis (2018) demonstrated that the enriched Loa component was largely absent from ~11–47 Ma, whereas the continuous record of shield magmatism was not modified. Therefore, it is not

the nature of the dry mantle of the shield reservoir that determines the volume of the shield magmatism but rather the volume of melts derived from the filaments generated at 5 GPa. The geochemical signature is the fingerprint of the mantle composition within the shield reservoir. Regardless, it is likely that the distribution of filaments inside the plume is heterogeneous. This is suggested by Ballmer *et al.* (2013) who proposed that the northern side of the Hawaiian chain is characterized by a higher volume of melt, which can be linked to the higher volume of filaments in the northern side of the Hawaiian plume (e.g. Yu *et al*., 2018).

*Postshield volcanism***.** The postshield magmas are typically small volume alkaline melts erupting immediately after (and sometimes overlapping with) the shield-stage magmas of some Hawaiian volcanoes (e.g. Clague, 1987a; Haase *et al*., 2019). Farnetani and Hofmann (2010) suggested that they represent deeper melts than shield magmas, the latter forming at depths >4 GPa in the garnet peridotite field. This suggestion agrees with their lower SiO_2 content and higher $(Ce/Yb)_N$ than those of most shield melts (Haase *et al*., 2019). Rhodes (2016), on the other hand, proposed that the former originated by a garnet-free melting of the mantle at a relatively shallow depth (< 3 GPa). This assertion was based on the characteristics of postshield lavas from Mauna Kea, Kohala and Hualalai, especially their higher Al_2O_3 content relative to shield-stage lavas. Our model could reconcile these two divergent interpretations if we consider that dykes arriving from the melting zone (5 to 4 GPa depth) and transporting postshield magmas may or may not interact with the shield reservoir. If they do not interact, they will maintain the imprint of their genesis in the garnet peridotite stability field, whereas if they do interact, they lose those imprints owing to the reaction with shield reservoir products.

The postshield activity of two volcanic sites, Mahukona and Haleakala, are not compatible with the volcanic classification of Clague (1987) and Clague & Dalrymple (1987). Both sites clearly show a delay to the start of their activity compared to their postshield stage. At Mahukona, the

postshield stage lasts till 325 ± 25 ka, whereas the shield stage ends at ~400 ka (Clague & Calvert, 2009). It implies that the postshield stage may be related to melts provided to the subsurface by the Hawaiian plume from outside the shield magmatic reservoir ~325 ky ago. In particular, at that time, the axis of the plume was located 24 km downflow of its present position at a distance to the Mahukona volcano, clearly within the 100 to 150 km interval where melt trajectories initiated at 150 km depth drive out to pond within the shield magma reservoir (Fig. 6a). This idea explains that the volcanism around 0.3 Ma at Mahokona can be compared with that of the preshield stage of Loihi (Garcia *et al.*, 2012).

"Downflow-postshield volcanism." The situation is more complex for Haleakala volcanism. The lavas of the submarine Hana Ridge, on which the Haleakala volcano rests, are tholeiitic basalts and picrites, similar to lavas from the Kilauea shield-building stage (Ren *et al*., 2004). The postshield stage began with Kula volcanism, composed essentially of hawaiites and dated at 1 Ma to 0.15 Ma, followed by the still-active Hana volcanism. The latter is characterized by alkaline lavas such as basanites. The closest volcano is the extinct Kohala shield volcano located 100 km from Haleakala and which began its activity ~1 Ma (Fig. 7a). It can be inferred that when Kula volcanism was initiated, the plume lay in the immediate vicinity of Kohala, i.e. 100 km from Haleakala. It is thus reasonable to assume that dykes transporting the erupted melts avoided ponding in the active shield magma reservoir underneath Kohala during this period. These dykes probably emerged near the subsurface below Haleakala. Further, it is tempting to assume that the recent Hana volcanism is related to the present plume, now located at ~160 km from Haleakala. Phillips *et al.* (2016) studied the isotopic composition of the nepheline-normative basanites from the Hana suite. These basanites are enriched in incompatible trace elements and have a more depleted isotopic signature than the similarly aged Hawaiian shield lavas from Kilauea and Mauna Loa. These differences relate to the time needed for the parental mantle melt of the Hana lavas to reach the subsurface, this time being ~20×

greater than that necessary for the Kilauea and Mauna Loa shield lavas. Our model explains this through the dykes generated at ~150 km from the plume axis and that likely root at 120 km along the hot flowline trajectory (Fig. 4b). These melts were produced at 150 km and 50 km from the plume axis and were thereafter transported via ductile plume flow before being eventually transported to the subsurface through dykes generated at 150 km from the plume axis (Figs 1d, 3c and 4b). It is clear that the time required for the melt to move 50 to 150 km away from the plume axis requires ~1 Ma, an order of magnitude greater than the 0.1 My needed for the melt produced at 150 km depth along the plume axis to erupt at the surface (Fig. 3). Accordingly, the trace element and depleted isotopic signatures of the Hana lavas are explained by the specific trajectory of their parental melt within the mantle. We thus propose that the postshield volcanism of Mahukona and Haleakala is caused by about 20% of the tholeiite-picrite and meimechite-like primitive melts produced within the hot centre of the plume not ponding within the shield magma reservoir centred along this hot centre of the plume. To distinguish this new type of Hawaiian volcanism represented by this pair of volcanoes from the normal postshield volcanism at the border of the shield magma reservoir, we designate this type as downflow-postshield volcanism.

The evolution of He^3/He^4 along the Hawaiian chain

The observation of $^3He/^4He$ ratios at more than eight times the Ra atmospheric record and a $\mu^{182}W$ ~0 provide evidence of a major role for sub-primitive mantle filaments or particularly old, i.e. a few Ga, fertilized-harzburgite source to generate most lavas along the Hawaiian chain. Regarding the latter, some incompatible trace element ratios, such as Nb/U, appear to agree with the occurrence of such a type of fertilized-harzburgite source (Hofmann, 1986). This is illustrated in particular by the east-to-west decrease of $^3He/^4He$ in lavas along the chain. For instance, Loihi preshield lavas have the highest helium ratio values, sometimes more than 30 ×

Ra in tholeiitic samples, whereas transitional, alkaline to basanitic samples have an elevated but relatively lower helium ratio (>20 × Ra) (Staudigel *et al*., 1984). These observations support the idea that melts from dykes avoid the shield magma reservoir and only pond below the crust. Thus, some tholeiites derived from the melting of sub-primitive mantle or old fertilized filaments may not eventually mix with other melts when they erupt at the surface through the Loihi fracture. During the shield stage, the helium ratio decreases from ~20 × Ra to ~8 × Ra from the time of construction of the volcano to the end of the shield stage (Kurz *et al*., 1987). This is consistent with the idea that during their ponding period as sills in the shield magma reservoir, the mixing of tholeiite-picrite melts (high $^{3}He/^{4}He$) with meimechite-like melts derived from the partial melting of a low $^{3}He/^{4}He$ and recent (<1 Ga) filament or interaction with the dry peridotite mantle lithosphere (8 × Ra) promoted a drop from a ratio of 30 × Ra (the maxima at Loihi) to 20 × Ra (value obtained after magma differentiation in chambers below Loihi). On the other hand, we propose that values as low as 8 × Ra agree well with a preferential accumulation of meimechite-like melts associated with a recent fertilized hazburgite in the subcrustal magma reservoir below the main island at the end of shield magma reservoir activity. These low values match those of alkaline and transitional basaltic, ankaramite, hawaiite, mugearite, benmoreite and trachyte melts, which characterize the postshield stage (Clague, 1987). Although this type of volcanism represents a very small fraction of the total volume of the Hawaiian volcanism, its occurrence is a strong argument that melts provided by young fertilized-harzburgite filaments effectively contribute to the Hawaiian volcanism. However, downflow-postshield volcanism at Mahukona and Haleakala represent a striking exception to the monotonic decrease of the $^{3}He/^{4}He$ ratio with distance from Kilauea, as they display lavas and xenoliths having a $^{3}He/^{4}He$ ratio of 21 Ra and 32 Ra, respectively, i.e. similar to those observed for the Loihi preshield lavas (Garcia *et al*., 1990; Rison & Craig, 1983). This last

observation is consistent with dykes that provide the subcrust melt at downflow-postshield volcanoes not interacting with the shield magma reservoir.

Finally, the He^3/He^4 of rejuvenated lavas is commonly low (ranging between 7 × Ra to 9 × Ra) except at South Arch, where the values range between 16 × Ra and 22 × Ra, i.e. a ratio similar to that of the shield stage. This observation requires an explanation within the framework of our model. We propose linking the 7 × Ra to 9 × Ra range to a possible infiltration of a carbonatitic (or kimberlitic) melt that concentrates inside young fertilized-harzburgite filaments (≤1 Ga; He^3/He^4 ~0) that flow along the weakly tilted section of the cold flowline (Fig 4b). From laboratory experiments, we see that the infiltration process of carbonatites behaves as a diffusive process, having an equivalent diffusivity D of 4.10^{-9} m^2/s and 5.10^{-8} m^2/s when reacting with olivine or pyroxene minerals, respectively, within the overriding mantle (Shatskiy *et al*., 2013). It is deduced that a diffusion front develops on the dry peridotitic horizon (He^3/He^4 = 7–9 × Ra), which caps the filaments at the height of $\sim\sqrt{Dt}$, where t represents the time elapsed between the generation of the carbonatitic impregnation at 75 km from the plume axis to its discharge via dykes at ~200 km from that axis. According to our model, when t ~1.2 Ma and $\sqrt{Dt}$ = 500 to 1500 m when the carbonatite melt interacts with a dry peridotite, the He^3/He^4 of reacting melt increases close to 7–9 × Ra. At the same time, because the carbonatitic melt—initially confined in a filament—infiltrates its overlying dry mantle cap, the mush percolates upward through this infiltrated front (Keller & Katz, 2016). According to Shatskiy *et al.* (2013), such a process likely leads to an increase in the height of the infiltration front by approximately an order of magnitude, i.e. 5 to 15 km. Such a distance is sufficient to buffer the He^3/He^4 of the carbonatitic melt to the value of the dry mantle cap. We note that deep xenoliths brought to the surface at Oahu likely show the imprint of such an infiltration process related to carbonatitic/kimberlitic melts (see, for example, Fig. 1 in Keshav & Sen (2003) and Plate 17a in Sen (1987)). Further, the rejuvenated magmas from Molokai, Oahu, Kauai and Niihau, which

have He^3/He^4 values from 7 to 9 × Ra, i.e. in the range of the values of tholeiitic melts from mid-oceanic ridges centred on 8 × Ra (Poreda *et al*. 1986 and Hofmann *et al*., 2011), can be explained by a reacting carbonatite (or kimberlite). This hypothesis is consistent with that of Bizimis *et al.* (2005), who interpreted Salt Lake (Oahu) mantle xenoliths as originating from old, depleted, recycled lithosphere, and DeFelice *et al.* (2019), who generalized these results to rejuvenated volcanism occurring along the Hawaiian chain. Finally, the South Arch rejuvenated lavas, which occur outside and somewhat upflow of the Hawaiian track are the only rejuvenated lavas that show a high $^3He/^4He$, ranging between 16 × Ra and 22 × Ra. We propose that these rejuvenated lavas originate from a sub-primitive/ULVZ mantle filament, which is expected to have a high $^3He/^4He$.

CONCLUSIONS

1- In our plume model, four types of volatiles-rich filaments are considered; sub-primitive mantle, ultralow-velocity zone, fertilized-harzburgite and eclogite type filaments. The partial melting process exclusively occurs within those filaments.

2- The obstruction of the upward percolation of the partial melting-derived melts at the base of the lithosphere causes a series of propagating dykes. From the stress field, we distinguish two types of dykes. The first is generated at ~120 km depth and at a distance greater than 40 km from the plume axis and crosses the entire mantle section of the lithosphere before ponding below the crust at least at 100 km from the plume axis. The second type is generated at the same depth at a distance less than 40 km from the plume axis and ponds within the lithosphere at a depth ranging between 50 and 70 km, this final ponding horizon is called the shield magma reservoir.

3- The dykes genenrated at the top of hot flowlines carry melts resulting from almost complete melting of fertilized-harzburgite filaments. The composition of those melts is

similar to that of meimechites; which in our model is compatible with the prediction of high-MgO and volatile-rich melts rarely being erupted at the surface. On the other hand, 20% partial melting of the sub-primitive/ULVZ filaments result in primary tholeiite-picrite melts.

4- The dykes generated at the top of cold flowlines are linked to the rejuvenated volcanism. The composition of melt is kimberlite/carbonatite-like, resulting from few percent of melting regardless of the type of filaments.

ACKNOWLEDGMENTS

We appreciated the constructive reviews by Prof. M. Norman, Prof. T. Gerya, Prof. N. Sleep and an anonymous reviewer, which significantly improved the paper. We also greatly thank G. Zellmer, who also helped to greatly improve the present paper. Finally, we thank A. Cousin, the graphic designer of the GET laboratory, for drawing the figures and M. Hay (Maxafeau Scientific Editing) who revised and corrected the English.

DATA AVAILABILTY

No new data were generated in support of this research.

SUPPLEMENTARY MATERIALS

Supplementary materials are available at Journal of Petrology online.

REFERENCES

Agius, M. R., Rychert, C. A., Harmon, N. & Laske, G. (2017). Mapping the mantle transition zone beneath Hawaii from Ps receiver functions: Evidence for a hot plume and cold mantle downwellings. *Earth and Planetary Science Letters* 474, 226-236.

Agrusta, R., Goes, S. & Van Hunen, J. (2017). Subducting-slab transition-zone interaction: Stagnation, penetration and mode switches. *Earth and Planetary Science Letters*, *464*, 10-23.

1194 Allegre C.J. & Turcotte D.L. (1986). Implication of a two-component marble-cake mantle.
1195 *Nature* 323, 123-127.

1196 Andrault D., Pesce G., Bouhifd, M.A., Bolfan-Casanova N. & Hénot J.M. (2014). Melting of
1197 subducted basalt at the core-mantle boundary. *Science* 344 , 892-895.

1198 Ballmer M.D., Ito G., Wolfe C.J. & Solomon S.C. (2013). Double layering of a thermochemical
1199 plume in the upper mantle beneath Hawaii. *Earth and Planetary Science Letters* 376, 155-164.

1200 Barraud J., Gardien V., Allemand P. & Grandjean P. (2004). Analogue models of melt-flow
1201 networks in folding migmatites. *Journal of Structural Geology* 26 (2), 307-324

1202 Bercovici D. & Karato S.I. (2005). Mantle transition zone water filter. *McGraw-Hill Yearbook*
1203 *of Science and Technology*, 193-196.

1204 Bianco T.A., Ito G., Becker J.M. & Garcia M.O. (2005). Secondary Hawaiian volcanism
1205 formed by flexural arch decompression, *Geochemistry Geophysics Geosystems*, 6,
1206 doi:10.1029/2005GC000945

1207 Bianco, T. A., Ito, G., van Hunen, J., Ballmer, M. D., & Mahoney, J. J. (2008). Geochemical
1208 variation at the Hawaiian hot spot caused by upper mantle dynamics and melting of a
1209 heterogeneous plume. *Geochemistry, geophysics, geosystems*, *9*.

1210 Bizimis M., Sen G., Salters V.J.M. & Keshav S. (2005). Hf-Nd-Sr isotope systematics of garnet
1211 pyroxenites from Salt Lake Crater, Oahu, Hawaii: Evidence for a depleted component in
1212 Hawaiian volcanism. *Geochimica et Cosmochimica Acta* 69, 2629–2646.

1213 Brandon, A.D., Norman, M.D., Walker, R.J. and Morgan, J.W., 1999. 186Os–187Os
1214 systematics of Hawaiian picrites. *Earth and Planetary Science Letters*, 174, 25-42.

1215 Breuer, D., & Spohn, T. (1995). Possible flush instability in mantle convection at the
1216 Archaean–Proterozoic transition. *Nature*, *378*(6557), 608-610.

1217 Brey G.P., Bulatov V.K. & Girnis A.V. (2009). Influence of water and fluorine on melting of
1218 carbonated peridotite at 6 and 10 GPa. *Lithos* 112, 249-259.

1219 Ceuleener G. & Rabinowicz M. (1992). Mantle flow and melt migration beneath oceanic ridges:
1220 models derived from observations in ophiolites. *Washington, DC, American Geophysical Union*
1221 *Geophysical Monograph Series* 71, 123-154.

1222 Chen, C. H., Presnall, D. C., & Stern, R. J. (1992). Petrogenesis of ultramafic xenoliths from
1223 the 1800 Kaupulehu flow, Hualalai volcano, Hawaii. *Journal of Petrology* 33, 163-202.

1224 Christensen, U. (1984). Convection with pressure-and temperature-dependent non-Newtonian
1225 rheology. *Geophysical Journal International*, *77*(2), 343-384.

1226 Clague D.A. & Calvert A.T. (2009). Postshield stage transitional volcanism on Mahukona
1227 Volcano, Hawaii. *Bulletin of Volcanology* 71:533–539

1228 Clague D.A. (1987) Hawaiian xenolith populations, magma supply rates, and xenolith
1229 populations. *Bulletin of Volcanology* 53, 577–587

1230 Clague, D. A. & Dalrymple, G. B. (1987). The Hawaiian-Emperor volcanic chain, Part 1:
1231 Geological evolution. In: Decker, R. W., Wright, T. L. & Stauffer, P. H. (eds) Volcanism in
1232 Hawaii, *US Geological Survey, Professional Papers* 1350, 5-54.

1233 Clague, D.A. & Sherrod, D.R., (2014). Growth and degradation of Hawaiian volcanoes.
1234 Chapter3. In: Poland, M.P., Takahashi, T.J., Landowski, C.M. (Eds.), Characteristics of
1235 Hawaiian Volcanoes. *U.S. Geological Survey Professional Paper* 1801, pp. 97–146

1236 Clague, D.A. (1987). Hawaiian alkaline volcanism. *Geological Society, London, Special*
1237 *Publications* 30, 227-252.

1238 Coffin M. & Eldholm O. (1994). Large igneous provinces: Crustal structure, dimensions, and
1239 external consequences. *Reviews of Geophysics* 32(1):1-36.

1240 Collerson K.D., Williams Q., Ewart A.E. & Murphy D.T. (2010). Origin of HIMU and EM-1
1241 domains sampled by ocean island basalts, kimberlites and carbonatites: The role of CO2-fluxed
1242 lower mantle melting in thermochemical upwellings. *Physics of the Earth and Planetary*
1243 *Interiors* 181, 112–131

1244 Connolly, J. A. D. & Podladchikov Y. Y. (1998). Compaction-driven fluid flow in viscoelastic
1245 rock, *Geodinamica Acta* 11, 55– 84.

1246 Connolly, J. A. D. & Podladchikov Y. Y. (2007). Decompaction weakening and channeling
1247 instability in ductile porous media: Implications for asthenospheric melt segregation, *Journal*
1248 *of Geophysical Research-Solid Earth*, 112, B10205.

1249 Cordery M.J., Davies G.F. & Campbel I.H. (1997). Genesis of flood basalts from eclogite-
1250 bearing mantle plumes. *Journal of Geophysical Research-Solid Earth*, 102(B9), 20,179-20,197.

1251 Dalton J.A. & Presnall D.C. (1998). Carbonatitic melts along the solidus of model lherzolite in
1252 the system CaO-MgO-Al2O3-SiO2-CO2 from 3 to 7 GPa. *Contributions to Mineralogy and*
1253 *Petrology*,131,123–135.

1254 Dasgupta, R. & Hirschmann, M. M. (2006). Melting in the Earth's deep upper mantle caused
1255 by carbon dioxide. *Nature* 440, 659-662.

1256 Dasgupta, R., & Hirschmann, M. M. (2007). Effect of variable carbonate concentration on the
1257 solidus of mantle peridotite. *American Mineralogist* 92, 370-379.

Dasgupta, R., Hirschmann, M.M. & Stalker, K. (2006). Immiscible transition from carbonate-rich to silicate-rich melts in the 3 GPa melting interval of eclogite+CO2 and genesis of silica-undersaturated ocean island lavas. *Journal of Petrology*. 47, 647–671.

Dawson, J.B., Smith, J.V. & Hervig, R.L. (1980). Heterogeneity in upper-mantle lherzolites and harzburgites: *Royal Society of London Philosophical Transactions* 297, 323–332.

DeFelice C., Mallick S., Saal A. E. & Huang S. (2019). An isotopically depleted lower mantle component is intrinsic to the Hawaiian mantle plume. *Nature Geoscience* 12, 487–492.

Dixon, J. E., Leist L., Langmuir C. & Schilling J.-G. (2002). Recycled dehydrated lithosphere observed in plume-influenced mid-ocean-ridge basalt. *Nature* 420, 385–389.

Dixon, J.E., Clague, D.A.,Wallace, P. & Poreda, R. (1997). Volatiles in alkalic basalts from the North Arch volcanic field, Hawaii: extensive degassing of deep submarine-erupted alkalic series lavas. *Journal of Petrology* 38, 911–939.

Dobretsov N.L. & Shatskiy A.F. (2012). Deep carbon cycle and geodynamics: the role of the core and carbonatite melts in the lower mantle. Russian Geology and Geophysics 53, 1117-1132.

Dubuffet, F., Rabinowicz, M., & Monnereau, M. (2000). Multiple scales in mantle convection. *Earth and Planetary Science Letters*, *178*(3-4), 351-366.

Elthon D. (1992). Chemical trends in abyssal peridotites: Refertilization of depleted suboceanic mantle. *Journal of Geophysical Research-Solid Earth* 97(B6), 9015-9025.

Ernst, R. (2014). Large Igneous Provinces. In Large Igneous Provinces (pp. I-Ii). Cambridge: Cambridge University Press, 653 pp.

Faccenda M. (2014). Water in the slab: A trilogy. *Tectonophysics* 614, 1-30.

Farnetani C. G. & Hofmann, A. W. (2010). Dynamics and internal structure of a lower mantle plume conduit. *Earth and Planetary Science Letters* 282, 314-322.

Farnetani C. G., Hofmann A. W., Duvernay T. & Limare A (2018). Dynamics of rheological heterogeneities in mantle plumes. *Earth and Planetary Science Letters* 499, 74–82.

Farnetani, C. G., Legras, B. & Tackley, P. J (2002). Mixing and deformation in mantle plumes. *Earth and Planetary Science Letters* 196, 1–15.

French S.W. & Romanowicz B. (2015). Broad plumes rooted at the base of the Earth's mantle beneath major hotspots. *Nature* 525, 95–99.

1288 Frey, F. A. & Clague, D. A. (1983). Geochemistry of diverse basalt types from Loihi Seamount,
1289 Hawaii: petrogenetic implications. *Earth and Planetary Science Letters* 66, 337-355.

1290 Frey, F. A., & Rhodes, J. M. (1993). Intershield geochemical differences among Hawaiian
1291 volcanoes: Implications for source compositions, melting process and magma ascent
1292 paths. *Philosophical Transactions of the Royal Society of London. Series A: Physical and*
1293 *Engineering Sciences* 342, 121-136.

1294 Garcia M. O, Kurz M. D. & Muenow D. W. (1990) Mahukona: The missing Hawaiian volcano.
1295 *Geology* 18, 1111–1114.

1296 Garcia M. O., Hanano D., Flinders A., Weis D., Ito G. & Kurz M. D. (2012). Age, geology,
1297 geophysics, and geochemistry of Mahukona Volcano, Hawai`i. *Bulletin of Volcanology* 74,
1298 1445–1463.

1299 Garcia M. O., Tree J. P., Wessel P. & Smith J. R. (2020). Pūhāhonu: Earth's biggest and hottest
1300 shield volcano. *Earth and Planetary Science Letters* 542, 116296.

1301 Garcia M. O., Weis D., Jichac B. R., Ito G. & Hanano D. (2016). Petrology and geochronology
1302 of lavas from Ka‘ula Volcano: Implications for rejuvenated volcanism of the Hawaiian mantle
1303 plume. *Geochimica et Cosmochimica Acta* 185, 278-301

1304 Gasparik, T. (1990). Phase relations in the transition zone. *Journal of Geophysical Research:*
1305 *Solid Earth*, *95*(B10), 15751-15769.

1306 Gerbault M., Fontaine F. J., Rabinowicz M. & Bystricky M. (2017). Elastic flexure controls
1307 magma trajectories and explains the offset of primary volcanic activity upstream of mantle
1308 plume axis at la Reunion and Hawaii hotspot islands. *Earth and Planetary Science Letters* 462,
1309 142-156.

1310 Ghosh S., Litasov K. & Ohtani E. (2014). Phase relations and melting of carbonated peridotite
1311 between 10 and 20 GPa: a proxy for alkali- and CO2-rich silicate melts in the deep mantle.
1312 *Contributions to Mineralogy and Petrology* 167, 964.

1313 Gill, J.B. (1981). Orogenic andesites and plate tectonics. *Springer-Verlag, New York*, 390 p.

1314 Green D. H. (2015). Experimental petrology of peridotites, including effects of water and
1315 carbon on melting in the Earth’s upper mantle. *Physics and Chemistry of Minerals* 42, 95–122.

1316 Grégoire M., Bell D.R. & Le Roex A.P. (2002). Trace element geochemistry of phlogopite-rich
1317 mafic mantle xenoliths: their classification and their relationship to phlogopite-bearing
1318 peridotites and kimberlites revisited. *Contributions to Mineralogy and Petrology* 142, 603–625.

1319 Grégoire M., Rabinowicz M. & Janse A.J.A. (2006). Mantle mush compaction: a key to
1320 understand the mechanisms of concentration of kimberlite melts and initiation of swarms of
1321 kimberlite dykes. *Journal of Petrology* 47, 631-646.

1322 Griggs RW. & Jones AT. (1997). Uplift caused by lithospheric flexure in the Hawaiian
1323 Archipelago as revealed by elevated coral deposits. *Marine Geology* 141, 11-25.

1324 Hacker, B. R., Abers, G. A., & Peacock, S. M. (2003). Subduction factory 1. Theoretical
1325 mineralogy, densities, seismic wave speeds, and H2O contents. *Journal of Geophysical*
1326 *Research: Solid Earth 108*(B1).

1327 Hacker, B. R., Peacock, S. M., Abers, G. A., & Holloway, S. D. (2003). Subduction factory 2.
1328 Are intermediate-depth earthquakes in subducting slabs linked to metamorphic dehydration
1329 reactions?. *Journal of Geophysical Research: Solid Earth*, *108*(B1).

1330 Hammond W.C. & Humphreys E.D. (2000). Upper mantle seismic wave velocity. Effects of
1331 realistic partial melt geometries. *Journal of Geophysical Research* 105 (B5), 10,975-10,986.

1332 Harpp, K. S., & Weis, D. (2020). Insights into the origins and compositions of mantle plumes:
1333 A comparison of Galápagos and Hawai'i. *Geochemistry, Geophysics, Geosystems*, *21*(9),
1334 e2019GC008887.

1335 Harrison, L. N., Weis, D., & Garcia, M. O. (2017). The link between Hawaiian mantle plume
1336 composition, magmatic flux, and deep mantle geodynamics. *Earth and Planetary Science*
1337 *Letters*, *463*, 298-309.

1338 Herzberg C., Condie K. & Jun Korenaga J. (2010). Thermal history of the Earth and its
1339 petrological expression. *Earth and Planetary Science Letters* 292, 79–88.

1340 Herzberg, C. & Asimow, P. D. (2015). PRIMELT3 MEGA.XLSM software for primary magma
1341 calculation: Peridotite primary magma MgO contents from the liquidus to the solidus.
1342 *Geochemistry, Geophysics, Geosystems* 16 (2), 563-578.

1343 Hirschmann M.M. (2000). Mantle solidus: Experimental constraints and the effects of
1344 peridotite composition. *Geochemistry, Geophysics, Geosystems* 1(10).

1345 Hirschmann, M. M. (2006). Water, melting, and the deep Earth H2O cycle. *Annu. Rev. Earth*
1346 *Planet. Sci.* 34, 629-653.

1347 Hirth G. & Kohlstedt D.L. (1995). Experimental constraints on the dynamics of the partially
1348 molten upper mantle: 2. Deformation in the dislocation creep regime. *Journal of Geophysical*
1349 *Research: Solid Earth* 100(B8), 15441-15449

1350 Hofmann A.W., Farnetani C.G. Spiegelman M. & Class C. (2011). Displaced helium and
1351 carbon in the Hawaiian plume. *Earth and Planetary Science Letters* 312, 226-236.

1352 Hofmann, A. W. (1986). Nb in Hawaiian magmas: constraints on source composition and
1353 evolution. *Chemical Geology* 57, 17-30.

1354 Jaques A. L. & Green D.H. (1980). Anhydrous melting of peridotite at 0–15 Kb pressure and
1355 the genesis of tholeiitic basalts. *Contributions to Mineralogy and Petrology* 73, 287–310.

1356 Karato S. & Wu P. (1993). Rheology of the upper mantle: A synthesis. *Science* 260 (5109),
1357 771-778.

1358 Katsura T., Yoneda A., Yamazaki D., Yoshino T. & Ito E. (2010). Adiabatic temperature profile
1359 in the mantle. *Physics of the Earth and Planetary Interiors* 183, 212-218.

1360 Katz R. F., Spiegelman M. & Langmuir C.H. (2003). A new parameterization of hydrous mantle
1361 melting. *Geochemistry, Geophysics, Geosystems* 4(9).

1362 Keshav S. & Sen G. (2003). A rare composite xenolith from Salt Lake Crater, Oahu: high-
1363 pressure fractionation and implications for kimberlitic melts in the Hawaiian mantle.
1364 *Contributions to Mineralogy and Petrology* 144, 548-558.

1365 Keshav S., Sen G. & Presnall D.C. (2007). Garnet-bearing Xenoliths from Salt Lake Crater,
1366 Oahu, Hawaii: High-Pressure Fractional Crystallization in the Oceanic Mantle. *Journal of*
1367 *Petrology* 48, 1681-1724.

1368 Kimura J.-I., Gill J. B., Skora S., van Keken P. E. & Kawabata H. (2016). Origin of geochemical
1369 mantle components: Role of subduction filter: Origin of Earth's geochemical components.
1370 Geochemistry Geophysics Geosystems 17(8).

1371 Kiseeva E. S., Vasiukov D.M, Wood B.J., McCammon C., Stachel T., Bykov M., Bykova E.,
1372 Chumakov A., Cerantola V., Harris J.W. & Dubrovinsky L. (2018). Oxidized iron in garnets
1373 from the mantle transition zone. *Nature Geoscience* 11 (2), 144-147.

1374 Klein F. W. (1982). Earthquakes at Loihi Submarine volcano and the Hawaiian Hot Spot.
1375 *Journal of Geophysical Research: Solid Earth* 87(B9), 7719-7726

1376 Kono Y., Kenney-Benson C., Hummer D., Ohfuji H., Park, C., Shen G., Wang Y., Kavner A.
1377 & Manning C. R. (2014). Ultralow viscosity of carbonate melts at high pressures. *Nature*
1378 *Communications* 5, 509.

1379 Kurz MD., Jenkins WJ., Hart SR. & Clague DA. (1983) Helium isotopic variations in volcanic
1380 rocks from Loihi Seamount and the island of Hawaii. *Earth and Planetary Science Letters* 66,
1381 388–406.

1382 Kurz, M.D., Garcia, M.O., Frey, F.A. & O'Brien, P.A. (1987). Temporal helium isotopic
1383 variations within Hawaiian volcanoes: basalts from Mauna Loa and Haleakala. *Geochimica and*
1384 *Cosmochimica Acta* 51, 2905– 2914.

Lange, R.A., Cashman, K.V., Navrotsky, A. (1994). Direct measurements of latent heat during crystallization and melting of a ugandite and an olivine basalt. *Contributions to Mineralogy and Petrology* 118, 169-181

Laske G., Markee A., Orcutt J. A., Wolfe C. J., Collins J. A., Solomon S. C., Detrick R. S., Bercovici D. & Hauri E. H. (2011). Asymmetric shallow mantle structure beneath the Hawaiian Swell-evidence from Rayleigh waves recorded by the PLUME network. *Geophysical Journal International* 187, 1725–1742.

Li X., Kind R., Priestley K., Sobolev S. V., Tilmann F., Yuan X., Weber M. (2000). Mapping the Hawaiian plume conduit with converted seismic waves. *Nature* 405, 938–941.

Li Z., Li J., Lange R., Liu, J. & Militzer B. (2017). Determination of calcium carbonate and sodium carbonate melting curves up to Earth's transition zone pressures with implications for the deep carbon cycle. *Earth and Planetary Science Letters* 457, 395-402.

Litasov K. & Ohtani E. (2002). Phase relations and melt compositions in CMAS-pyrolite-H2O system up to 25 GPa. *Physics of the Earth and Planetary Interiors* 134, 105– 127.

Liu Z., Park J. & Karato S.-I. (2018). Seismic evidence for water transport out of the mantle transition zone beneath the European Alps. *Earth and Planetary Science Letters* 482, 93-104

Liu, L. G. (1993). Effects of H2O on the phase behavior of the forsterite-enstatite system at high pressures and temperatures: revisited. *Physics of the earth and planetary interiors*, *76*(3-4), 209-218.

Maaloe S. (2004). The solidus of harzburgite to 3 GPa pressure: the compositions of primary abyssal tholeiite. *Mineralogy and Petrology* 81, 1–17

Maccaferri F., Bonafede M. & Rivalta E. (2011). A quantitative study of the mechanisms governing dike propagation, dike arrest and sill formation. Journal of Volcanology and Geothermal Research 208, 39–50.

Mao, H. K., Hu, Q., Yang, L., Liu, J., Kim, D. Y., Meng, Y. & Mao, W. L. (2017). When water meets iron at Earth's core–mantle boundary. *National Science Review*, *4*(6), 870-878.

Marty B. (2012). The origins and concentrations of water, carbon, nitrogen and noble gases on Earth. *Earth and Planetary Science Letters* 313–314, 56-66.

McKenzie D. (1977). Surface deformation, gravity anomalies and convection. *Geophysical Journal International* 48 (2), 211-238.

McNamara A.K. (2019). A review of large low shear velocity provinces and ultra low velocity zones. *Tectonophysics* 760, 199-220.

1417 Motoki, M. H., & Ballmer, M. D. (2015). Intraplate volcanism due to convective instability of
1418 stagnant slabs in the mantle transition zone. *Geochemistry, Geophysics, Geosystems* 16, 538-
1419 551.

1420 Mundl-Petermeier A., Walker R.J., Fischer R.A., Lekic V., Jackson M.G. & Kurz M.D. (2020).
1421 Anomalous ^{182}W in high 3He/4He ocean island basalts: Fingerprints of Earth's core?
1422 Geochimica et Cosmochimica Acta 271, 194–211

1423 Nomura R., Hirose K., Uesugi K., Ohishi Y., Tsuchiyama A., Miyake A. & Ueno Y. (2014).
1424 Low Core-Mantle Boundary Temperature Inferred from the Solidus of Pyrolite. Science 343,
1425 522-525.

1426 Ohtani, E., Toma, M., Litasov, K., Kubo, T., & Suzuki, A. (2001). Stability of dense hydrous
1427 magnesium silicate phases and water storage capacity in the transition zone and lower
1428 mantle. *Physics of the Earth and Planetary Interiors*, *124*(1-2), 105-117.

1429 Panina L. I. & Motorina I. V. (2013). Meimechites, Porphyritic Alkaline Picrites, and
1430 Melanephelinites of Siberia: Conditions of Crystallization, Parental Magmas, and Sources.
1431 *Geochemistry International* 51, 109–128.

1432 Park J., Morgan J.K., Zelt C.A., Okubo P.G., Peters L. & Benesh V. (2007). Comparative
1433 velocity structure of active Hawaiian volcanoes from 3-D onshore–offshore seismic
1434 tomography. *Earth and Planetary Science Letters* 259, 500–516

1435 Persikov S., Bukhtiyarov P.G. & Sokol A.G. (2017). Viscosity of hydrous kimberlite and
1436 basaltic melts at high pressures. *Russian Geology and Geophysics* 58, 1093–1100.

1437 Phillips, E.H., Sims, K.W., Sherrod, D.R., Salters, V.J., Blusztajn, J. & Dulai, H. (2016). Iso-
1438 topic constraints on the genesis and evolution of basanitic lavas at Haleakala, Island of Maui,
1439 Hawaii. *Geochimica and Cosmochimica Acta* 195, 201–225.

1440 Pinel V. & Jaupart C. (2003). Magma chamber behavior beneath a volcanic edifice. *Journal of*
1441 *Geophysical Research-Solid Earth* 108 (B2), 2072.

1442 Pinel, V., Carrara, A., Maccaferri, F., Rivalta, E., & Corbi, F. (2017). A two-step model for
1443 dynamical dike propagation in two dimensions: Application to the July 2001 Etna
1444 eruption. *Journal of Geophysical Research: Solid Earth* 122, 1107-1125.

1445 Poreda, R., Schilling, J.-G. & Craig, H. (1986). Helium and hydrogen isotopes in ocean-ridge
1446 basalts north and south of Iceland. *Earth and Planetary Science Letters* 78, 1–17.

1447 Putirka, K. (1999). Melting depths and mantle heterogeneity beneath Hawaii and the East
1448 Pacific Rise: constraints from Na/Ti and rareearth element ratios. *Journal of Geophysical*
1449 *Research-Solid Earth* 104, 2817–2829.

Putirka, K. (2005). Mantle potential temperatures at Hawaii, Iceland, and the mid-ocean ridge system, as inferred from olivine phenocrysts:evidence for thermally-driven mantle plumes. *Geochemistry,Geophysics, Geosystems*.doi:10.1029/2005GCGC000915.

Rabinowicz M. & Ceuleneer G. (2005). The effect of sloped isotherms on melt migration in the shallow mantle: a physical and numerical model based on observations in the Oman ophiolite. *Earth and Planetary Science Letters* 229, 231-246.

Rabinowicz M. & Toplis M.J. (2009). Melt Segregation in the Lower Part of the Partially Molten Mantle Zone beneath an Oceanic Spreading Centre: Numerical Modelling of the Combined Effects of Shear Segregation and Compaction. *Journal of Petrology* 50, 1071-1106.

Rabinowicz M., Ceuleneer G. & Nicolas A. (1987). Melt segregation and flow in mantle diapirs below spreading centers: evidence from the Oman ophiolite. *Journal of Geophysical Research: Solid Earth* 92 (B5), 3475-3486.

Rabinowicz M., Genthon P., Ceuleneer G. & Hillairet M. (2001). Compaction in a mantle mush with high melt concentrations and the generation of magma chambers. *Earth and Planetary Science Letters* 188 (3-4), 313-328

Rabinowicz, M., Calvet, M., & Toplis, M. (2012). Possible layering of mantle convection at the top of the Iceland Hotspot: a crosscheck between 3-D numerical models and gravimetric, seismic and petrological data. *Geophysical Journal International* 188, 35-60.

Rabinowicz, M., Ceuleneer, G., Monnereau, M., & Rosemberg, C. (1990). Three-dimensional models of mantle flow across a low-viscosity zone: implications for hotspot dynamics. *Earth and planetary science letters*, *99*(1-2), 170-184.

Rabinowicz, M., Ricard, Y., & Grégoire, M. (2002). Compaction in a mantle with a very small melt concentration: Implications for the generation of carbonatitic and carbonate-bearing high alkaline mafic melt impregnations. *Earth and Planetary Science Letters* 203, 205-220.

Ramberg, H. (1955). Thermodynamics and kinetics of petrogenesis. Crust of the earth: *Geol. Soc. America Special Paper* 62, 431-448.

Räss L., Duretz T. & Podladchikov Y.Y. (2019). Resolving hydromechanical coupling in two and three dimensions: spontaneous channeling of porous fluids owing to decompaction weakening. *Geophysical Journal International* 218, 1591–1616.

Ren, Z.-Y., Takahashi, E., Orihashi, Y. & Johnson, K. T. M. (2004). Petrogenesis of tholeiitic lavas from the submarine Hana Ridge, Haleakala volcano, Hawaii. *Journal of Petrology* 45, 2067-2099.

Ribe, N.M. & Christensen, U.R. (1999). The dynamic origin of Hawaiian volcanism. *Earth and Planetary Science Letters* 171, 517–531.

Rigo, A., Adam, C., Grégoire, M., Gerbault, M., Meyer, R., Rabinowicz, M. & Bonvalot, S. (2015). Insights for the melt migration, the volcanic activity and the ultrafast lithosphere delamination related to the Yellowstone plume (Western USA). *Geophysical Journal International*, *203*(2), 1274-1301.

Ringwood, A. E., & Major, A. (1967). High-pressure reconnaissance investigations in the system Mg2SiO4-MgO-H2O. *Earth and Planetary Science Letters*, *2*(2), 130-133.

Rison, W. & Craig, H. (1983). Helium isotopes and mantle volatiles in Loihi Seamount and Hawaiian Island basalts and xenoliths. *Earth and Planetary Science Letters* 66, 407– 426.

Rosenthal A., Yaxley G.M., Green D.H., Hermann J., Istvan Kovacs I. & Spandler C. (2014). Continuous eclogite melting and variable refertilisation in upwelling heterogeneous mantle. *Scientific Reports*. 4, 6099; DOI:10.1038/srep06099.

Ross K., Elthon D., Hellebrand E. & Snow J. (2005). Melt re-fertilization in Hess Deep peridotites. Ofioliti 30 (2), 253-254.

Rubin A. M. (1990). A comparison of rift-zone tectonics in Iceland and Hawaii. *Bull. Volcanol. 52, 302-319.*

Rüpke, L. H., Morgan, J. P., Hort, M., & Connolly, J. A. (2004). Serpentine and the subduction zone water cycle. *Earth and Planetary Science Letters* 223, 17-34.

Sen G. (1987). Xenoliths associated with the Hawaiian hot spot. Mantle Xenoliths, *Wiley, New York*, 359−375.

Shatskiy A., Sharygin I.S., Gavryushkin P.N., Litasov K.D., Borzdov Y.M., Shcherbakova A.V., Higo Y., Funakoshi K.-I., Palyanov Y.N. & Ohtani E. (2013). The system K2CO3-MgCO3 at 6 GPa and 900–1450 °C. *American Mineralogist* 98, 1593–1603.

Shatskiy, A., Litasov, K. D., Borzdov, Y. M., Katsura, T., Yamazaki, D., & Ohtani, E. (2013). Silicate diffusion in alkali-carbonatite and hydrous melts at 16.5 and 24 GPa: Implication for the melt transport by dissolution–precipitation in the transition zone and uppermost lower mantle. *Physics of the Earth and Planetary Interiors* 225, 1-11.

Sherrod D.R., Nishimitsu Y. & Tagami T. (2003). New K-Ar ages and the geologic evidence against rejuvenated-stage volcanism at Haleakalā, East Maui, a postshield-stage volcano of the Hawaiian island chain. *Geological Society of America Bulletin* 115 (6), 683–694.

Sleep, N. H., Warren J. M. (2014). Effect of latent heat of freezing on crustal generation at low spreading rates. *Geochemistry, Geophysics, Geosystems* 15, 3161–3174.

Sobolev A.V., Hofmann A.W., Sobolev S.V. & Nikogosian I.K. (2005). An olivine-free mantle source of Hawaiian shield basalts. *Nature* 434, 590–597.

Sobolev A.V., Sobolev S.V., Kuzmin D.V., Malitch K.N. & Petrunin A.G. (2009). Siberian meimechites: origin and relation to flood basalts and kimberlites. *Russian Geology and Geophysics* 5, 999–1033.

Solomon, S. C., Sleep, N. H., & Richardson, R. M. (1975). On the forces driving plate tectonics: Inferences from absolute plate velocities and intraplate stress. *Geophysical Journal International* 42, 769-801.

Soltanmohammadi, A., Grégoire, M., Rabinowicz, M., Gerbault, M., Ceuleneer, G., Rahgoshay, M., & Benoit, M. (2018). Transport of volatile-rich melt from the mantle transition zone via compaction pockets: implications for mantle metasomatism and the origin of alkaline lavas in the Turkish–Iranian plateau. *Journal of Petrology* 59, 2273-2310.

Spera, F. J. (1987). Dynamics of translithospheric migration of metasomatic fluid and alkaline magma. In Mantle metasomatism *Academic Press London*, 1-20.

Stagno, V. & Frost, D.J. (2010). Carbon speciation in the asthenosphere: Experimental measurements of the redox conditions at which carbonate-bearing melts coexist with graphite or diamond in peridotite assemblages. *Earth and Planetary Science Letters* 300, 72–84.

Staudigel, H., Zindler A., Hart S.R., Leslie T., Chen C.-Y. & Clague D. (1984). The isotope systematics of a juvenile intraplate volcano: Pb, Nd, and Sr isotope ratios of basalts from Loihi Seamount, Hawaii. *Earth and Planetary Science Letters* 69, 13–29.

ten Brink, U.S. & Brocher T. M. (1988). Multichannel seismic evidence for variations in crustal thickness across the Molokai Fracture Zone in the mid-Pacific. *Journal of Geophysical Research-Solid Earth* 93, 1119-1130.

Tilmann, F.J., Benz H.M., Priestley K.F. & Okubo P.G. (2001). P-wave velocity structure of the uppermost mantle beneath Hawaii from travel time tomography. *Geophysical Journal International* 146, 594–606.

Tucker, J.M., Hauri, E.H., Pietruszka, A.J., Garcia, M.O., Marske, J.P. and Trusdell, F.A., 2019. A high carbon content of the Hawaiian mantle from olivine-hosted melt inclusions. *Geochimica et Cosmochimica Acta*, 254, 156-172.

van Arc E. & Lin J. (2004). Time variation in igneous volume flux of the Hawaii-Emperor hot spot seamount chain. *Journal of Geophysical Research-Atmospheres* 109(11).

Van Keken P.E., Ballentine C.J. & Hauri E.H. (2003). Convective mixing in the Earth's mantle. *Treatise on geochemistry* 2, 1-21.

Wallace P.J. (1998). Water and partial melting in mantle plumes: Inferences from the dissolved H2O concentrations of Hawaiian basaltic magmas. *Geophysical Research Letters* 25, 3639-3642.

Wark, D. A., & Watson, E. B. (1998). Grain-scale permeabilities of texturally equilibrated, monomineralic rocks. *Earth and Planetary Science Letters* 164, 591-605.

Watts A. B. & ten Brink U. (1989). Crustal Structure, Flexure, and Subsidence History of the Hawaiian Islands. *Journal of Geophysical Research-Atmospheres* 94, 10473-10500.

Weinberg R.F., Veveakis E. & Regenauer-Lieb K. (2015). Compaction-driven melt segregation in migmatites. *Geology* 43(6), 471–474.

Weis, D., Garcia, M. O., Rhodes, J. M., Jellinek, M., & Scoates, J. S. (2011). Role of the deep mantle in generating the compositional asymmetry of the Hawaiian mantle plume. *Nature Geoscience*, *4*(12), 831-838.

Weis, D., Harrison, L. N., McMillan, R., & Williamson, N. M. (2020). Fine-Scale Structure of Earth's Deep Mantle Resolved Through Statistical Analysis of Hawaiian Basalt Geochemistry. *Geochemistry, Geophysics, Geosystems*, *21*(11), e2020GC009292.

Wolfe C.J., Solomon S.C., Laske G., Collins J.A., Detrick R.S., Orcutt J.A., Bercovici D. & Hauri E.H. (2011). Mantle P-wave velocity structure beneath the Hawaiian hotspot. *Earth and Planetary Science Letters* 303, 267-280.

Wright T.L. & Klein F.W. (2006). Deep magma transport at Kilauea volcano, Hawaii. *Lithos* 87, 50–79.

FIGURE CAPTIONS

Fig. 1 Mantle plume convective model incorporating a viscoelastic lithosphere (Gerbault *et al*., 2017); (a) Isotherms, direction of maximum compression σ_1 (arrows with length proportional to stress amplitude) and colour code of the isocontours of "dynamic pressure," i.e., the difference between the mantle and the lithostatic pressure. Values in blue correspond to zones that are in dynamic compression, and values in red correspond to zones in depression; (b) isotherms and isocontours (in colour) of the effective viscosity of the mantle. Note that the base of the lithosphere follows approximatively the border of the intense blue zone, i.e. the ~ 10^{20} Pa·s horizon; (c) isotherms, vectors representing the convecting velocity (arrows, with length proportional to velocity amplitude) and isocontours of the temperature (in colour); (d) plume model characteristics necessary for understanding the melt-mantle separation processes. The 1500°C isotherm delimits the high temperature centre of the plume, and some velocity vectors

of the plume flow are drawn with directions of σ_1 throughout the plume and the overriding lithosphere. The elastically compressed zone, due to the flexion of the lithosphere (shown as red rectangular box), is designated in the text as the "shield magma reservoir." The solid red line presents the trajectory of the dyke bringing melt to the surface of preshield volcanoes. The melt is initiated at 5 GPa and at <40 km from the plume axis, then ponds in the shield magma reservoir and eventually emerges at the surface, 100 km from the plume axis. Dashed blue lines illustrate the hot and cold flowlines that follow the trajectory of the mantle at the border of the hot centre and cold boundary of the plume, respectively.

Fig. 2 Pressure (depth)-temperature diagram illustrating the different curves used in the present study. The solidus of the dry lherzolite (from Herzberg *et al*., 2000) is also estimated to be that of the fertilized harzburgite having 500 ppm H_2O. The solidus of dry fertilized harzburgite is estimated as the adjustment of the dry solidus by +150°C, whereas the dry lherzolite having 500 ppm H_2O is estimated as the same dry solidus reduced by 150°C. Lines in the figure include the solidi of i) vapour-saturated peridotite (from Green, 2015); ii) pyrolite having 2 wt.% H_2O (from Litasov & Ohtani, 2002); and iii) carbonate-bearing fertile peridotite (from Dasgupta *et al*., 2006). iv) The solidus and liquidus of eclogite (from Rosenthal *et al*., 2014) and v) the adiabatic temperature at the boundary and along the plume axis (from Katsura *et al*., 2010). The axial temperature profile is assumed to exceed the adiabatic profile by 280°C (Putirka, 2005). Estimates of the pyroxene-out of lherzolite having 500 ppm H_2O and the dry lherzolite at 3 GPa, 5 GPa and 8 GPa are deduced from Katz *et al.* (2003).

Fig. 3 a) Model by Räss *et al.* (2019) showing the development of elongated melt tubes when the interstitial melt concentration drops by a factor of 3 at 5 GPa and the viscosity of the mush drops by a factor of 500 when the excess pressure p_e is positive. The scale of the model is adapted to describe the percolation process of tholeiite–picrite melts formed around the plume

axis. b) Probable shape of the flowlines in the plume when the melt concentration exceeds ~5% in volume (from Rabinowicz & Toplis, 2009). This leads to a horizontal orientation of the direction of maximum compression σ_1. If the mush results from the superposition of spherical grains of equal size, the σ_1 stress leads to a horizontal coalescence of these grains, and the melt moves inside planes that separate successive horizons of coalesced grains. Such a process leads to a marked drop in the vertical permeability of the mush, which leads to a marked obstruction of the vertical melt percolation. In addition to considering that the mush deconsolidates when the interstitial melt concentration is high (~30%) and when p_e >0, Fig. 3a describes tholeiite–picrite melt concentration in tubes within the plume above the 5% partially molten horizon rooting at a depth of ~150 km (~5 GPa). Fig 3c displays (black lines) the trajectories of dykes that drain the melt concentrated at the top of the melt tubes. This melt develops in evenly distributed sub-primitive filaments inside the plume centre. They follow the orientation of σ_1 (black segments) and eventually pond below the crust within magma chambers (red ellipses). The different trajectories provide melts to preshield, shield, postshield and downflow-postshield volcanoes as described in the text. Fig 3d explains why—because of the elastic twist of the lithosphere induced by the underlying plume—sills lodged in the shield magma reservoir fold and generate dykes above 50 km to provide melt to shield volcanoes.

Fig. 4 Evolution (1D) of melt concentration related to the obstruction of upward melt percolation, which occurs at the bottom of the lithosphere (from Rabinowicz & Ceuleneer, 2005). The initial melt concentration profile of the computation is drawn in a thin plain line, above 420 km depth, where it is equal to ϕ_r, the initial melt/mush mass ratio. The bold plain line represents the evolution of melt concentration after 80 ka. Note that below the lithosphere, the uppermost compaction wave is ~30 km thick and reaches a maximum melt concentration of ~10ϕ_r**.** b) The trajectories of the dykes that develop at the top of the compaction waves and in which carbonatite/kimberlite-like melts are concentrated. This process stems from the

dehydration and decarbonation of the fertilized-harzburgite filaments above the mantle transition zone (see text). The intensity of interstitial melt concentration is represented by the colour gradient from intense red to light pink. Along the plume axis, a train of compaction waves develops because of the permeability drop at the base of the lithosphere. Away from the plume axis, in contrast, a train of compaction waves results from the horizontalization of flowlines due to the rotation of the flow below the lithosphere (see text). Inside the hot centre of the plume, the mantle in the upper wave melts completely to form meimechite-like melts that apply a pressure at the plume top to trigger dykes that follow the direction of σ_1 to transport the melt up to the base of the crust. The trajectories are very similar to those of sub-primitive filaments (Fig. 3) and thus feed the same volcanoes. Similarly, along the elbow formed by the cold flowline, carbonatitic melt may accumulate; however, because of the low temperature, fertilized-harzburgite filaments only experience moderate partial melting. The produced melt is channelled along the weakly tilted (to horizontal) arm of the elbow. The resulting kimberlite-like melt concentrates at its apex, where excess pressure is sufficient to promote melt transport via dykes up to the subcrust or even to the surface at a distance >200 km from the plume axis. This process explains rejuvenated volcanism (see text).

Fig. 5 *Vp* seismic anomalies (in %), derived from the Rayleigh wave tomographic model of Laske *et al*. (2012), at a) 60 km, b) 80 km and c) 140 km depth. d) *Vp* seismic anomalies (in %) at 65 km depth, as derived from the P-volume wave tomography model of Tillman *et al*. (2001). Note that the seismic anomalies are positive and represent local maxima above both the main island and the main shield volcanoes.

Fig. 6 Three-dimensional onshore–offshore *Vp* seismic tomography of the eastern margin of the main island (from Park *et al*., 2007), with velocity fields at a) 10 km and b) 12 km depth. A velocity <6 km/s corresponds to crustal material, whereas a velocity >6 km/s corresponds to

mafic or mantle materials. Also provided are the vertical velocity fields along the profiles c) AA′ (in Fig. 6a) and d) BB′ (in Fig. 6b). The positions of Mauna Loa, Loihi, Kilauea, Keikikea and Hohonu are indicated.

Fig. 7 a) Representation of the surface distribution of the loci of various earthquakes around the main island (from Tillman *et al*., 2001). The *Vp*-anomaly map at 10 km depth identifies the location of Lohihi and Keikikea volcanoes and associated seismic activity (the full map is displayed in Fig. 6a). Also provided is the distribution of the loci of earthquakes along a vertical plane linking b) Mauna Loa to Kilauea (Tillman *et al*., 2001) and c) Loihi to Kilauea (Klein, 1982).

Fig. 8 Model of Watts & ten Brink (1989) of the evolution of the Moho depth along the Hawaiian chain, including topography, positions of the top of the oceanic crust, base of the oceanic crust and depth of the Moho discontinuity along the axis of the Hawaiian chain. The numbers above the islands are the radiogenic ages of surface lavas (Clague & Dalrymple, 1987). The velocity–depth structure based on ESP 5 is also presented (ten Brink & Brocher, 1988).

Fig. 9 Diagrams illustrating the flow of various mantle materials of the Hawaiian plume along the Mauna Kea and Mauna Loa lines. The basic flow (cream color) is assumed to consist of dry peridotite; the light blue stripes represent devolatized LLSVP mantle, i.e. Loa-type mantle, and the red stripes represent devolatized Pacific, i.e. Kea-type mantle. Sub-primitive/ULVZ (deep blue), eclogite (yellow) and fertilized-harzburgite (grey) filaments are transported by the mantle flow and eventually partially melt beneath the lithosphere. The melts provided by filaments are collected in dykes rooting between 120 and 150 km depth and are eventually transported upward to pond in the shield reservoir and subcrustal magma chambers (preshield, postshield and downflow-postshield dykes) or directly erupt at the surface (rejuvenated dykes). It is important to note that the type of mantle composing the lithosphere depends on its nature when

it was integrated to the lithosphere during its subsidence, i.e., far from the present position of the plume. Because the type of mantle in the shield magma reservoir determines the Kea (light blue) or Loa (dark pink) nature of shield magma, it is deduced that, at present, the nature of the mantle within the shield reservoir and the sublithospheric plume flow is identical. This is not the case downflow of the plume, however, where the nature of mantle sources of shield melts fluctuates along both lines.

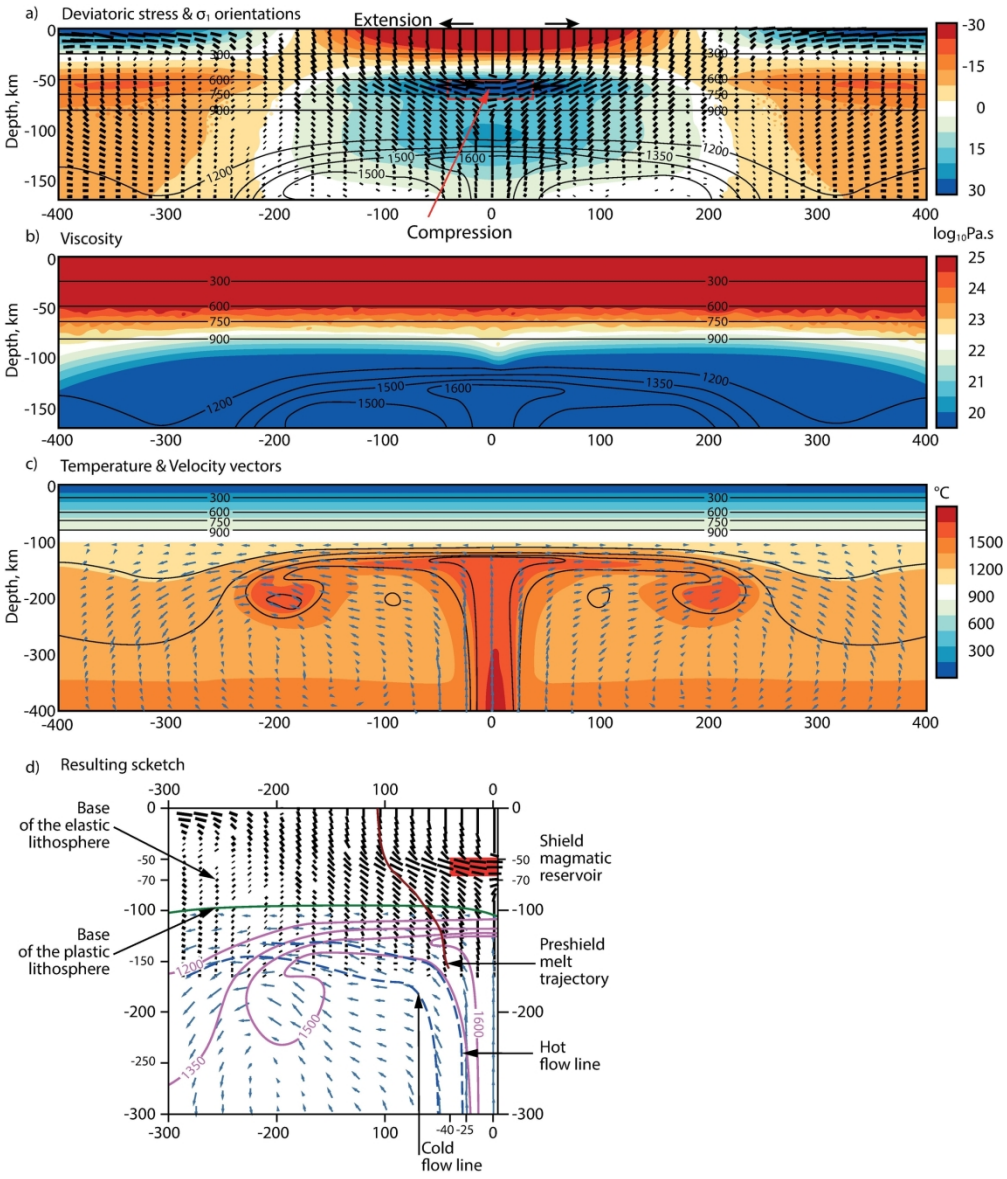

Fig. 1 Mantle plume convective model incorporating a viscoelastic lithosphere (Gerbault et al., 2017); (a) Isotherms, direction of maximum compression σ1 (arrows with length proportional to stress amplitude) and colour code of the isocontours of "dynamic pressure," i.e., the difference between the mantle and the lithostatic pressure. Values in blue correspond to zones that are in dynamic compression, and values in red correspond to zones in depression; (b) isotherms and isocontours (in colour) of the effective viscosity of the mantle. Note that the base of the lithosphere follows approximatively the border of the intense blue zone, i.e. the ~ 1020 Pa·s horizon; (c) isotherms, vectors representing the convecting velocity (arrows, with length proportional to velocity amplitude) and isocontours of the temperature (in colour); (d) plume model characteristics necessary for understanding the melt-mantle separation processes. The 1500°C isotherm delimits the high temperature centre of the plume, and some velocity vectors of the plume flow are drawn with directions of σ1 throughout the plume and the overriding lithosphere. The elastically compressed zone, due to the flexion of the lithosphere (shown as red rectangular box), is designated in the text as the "shield magma reservoir." The solid red line presents the trajectory of the dyke bringing melt to the surface of preshield volcanoes. The melt is initiated at 5 GPa and at <40 km from the plume axis, then ponds in the shield magma reservoir and eventually emerges at the surface, 100 km from the plume axis. Dashed blue

lines illustrate the hot and cold flowlines that follow the trajectory of the mantle at the border of the hot centre and cold boundary of the plume, respectively.

184x216mm (300 x 300 DPI)

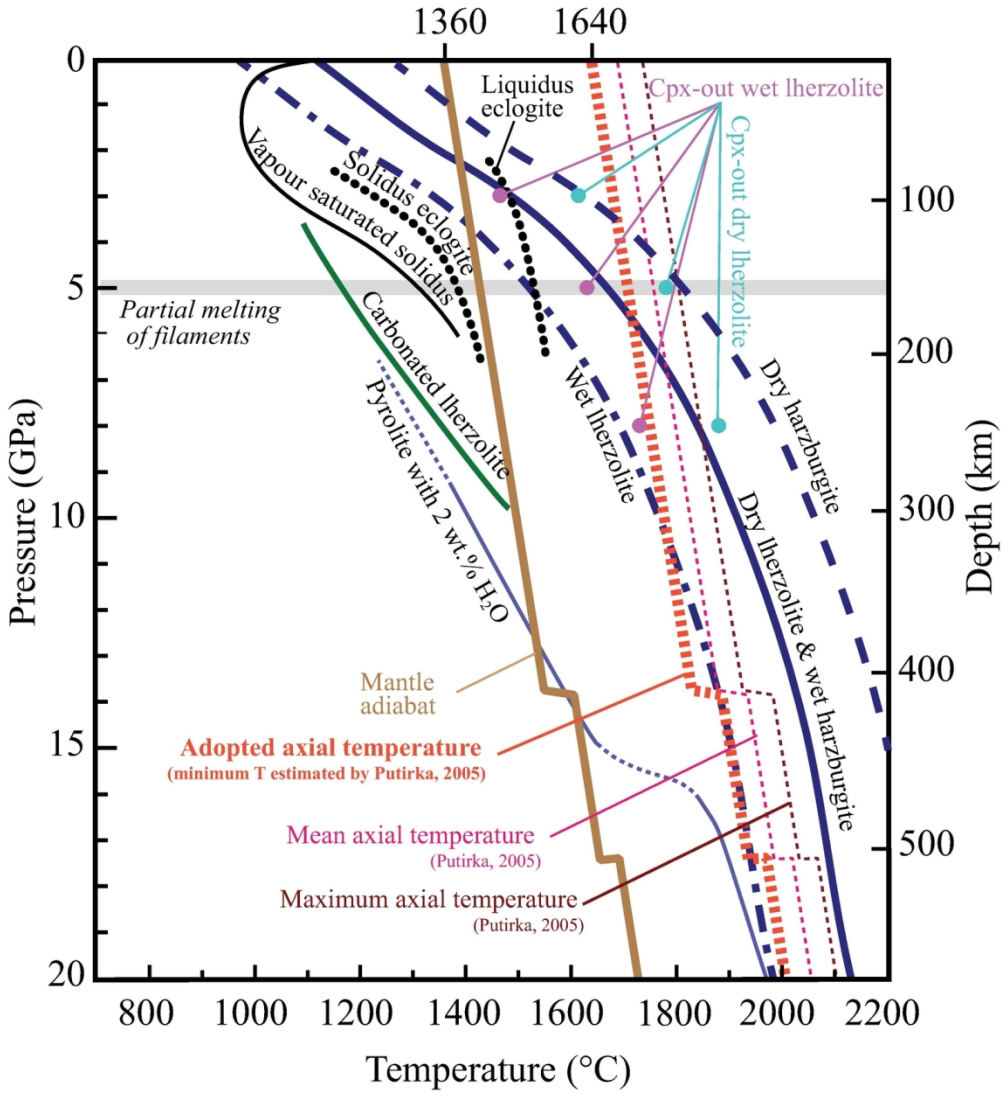

Fig. 2 Pressure (depth)-temperature diagram illustrating the different curves used in the present study. The solidus of the dry lherzolite (from Herzberg et al., 2000) is also estimated to be that of the fertilized harzburgite having 500 ppm H2O. The solidus of dry fertilized harzburgite is estimated as the adjustment of the dry solidus by +150°C, whereas the dry lherzolite having 500 ppm H2O is estimated as the same dry solidus reduced by 150°C. Lines in the figure include the solidi of i) vapour-saturated peridotite (from Green, 2015); ii) pyrolite having 2 wt.% H2O (from Litasov & Ohtani, 2002); and iii) carbonate-bearing fertile peridotite (from Dasgupta et al., 2006). iv) The solidus and liquidus of eclogite (from Rosenthal et al., 2014) and v) the adiabatic temperature at the boundary and along the plume axis (from Katsura et al., 2010). The axial temperature profile is assumed to exceed the adiabatic profile by 280°C (Putirka, 2005). Estimates of the pyroxene-out of lherzolite having 500 ppm H2O and the dry lherzolite at 3 GPa, 5 GPa and 8 GPa are deduced from Katz et al. (2003).

134x146mm (300 x 300 DPI)

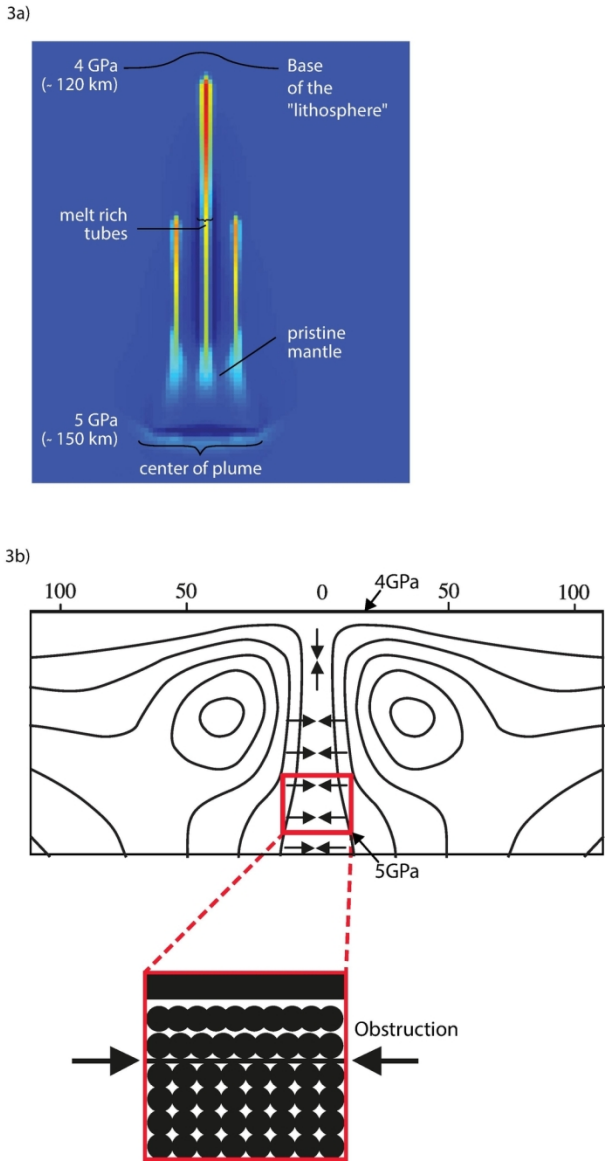

Fig. 3 a) Model by Räss et al. (2019) showing the development of elongated melt tubes when the interstitial melt concentration drops by a factor of 3 at 5 GPa and the viscosity of the mush drops by a factor of 500 when the excess pressure pe is positive. The scale of the model is adapted to describe the percolation process of tholeiite–picrite melts formed around the plume axis. b) Probable shape of the flowlines in the plume when the melt concentration exceeds ~5% in volume (from Rabinowicz & Toplis, 2009). This leads to a horizontal orientation of the direction of maximum compression σ1. If the mush results from the superposition of spherical grains of equal size, the σ1 stress leads to a horizontal coalescence of these grains, and the melt moves inside planes that separate successive horizons of coalesced grains. Such a process leads to a marked drop in the vertical permeability of the mush, which leads to a marked obstruction of the vertical melt percolation. In addition to considering that the mush deconsolidates when the interstitial melt concentration is high (~30%) and when pe >0, Fig. 3a describes tholeiite–picrite melt concentration in tubes within the plume above the 5% partially molten horizon rooting at a depth of ~150 km (~5 GPa). Fig 3c displays (black lines) the trajectories of dykes that drain the melt concentrated at the top of the melt tubes. This melt develops in evenly distributed sub-primitive filaments inside the plume

centre. They follow the orientation of σ1 (black segments) and eventually pond below the crust within magma chambers (red ellipses). The different trajectories provide melts to preshield, shield, postshield and downflow-postshield volcanoes as described in the text. Fig 3d explains why—because of the elastic twist of the lithosphere induced by the underlying plume—sills lodged in the shield magma reservoir fold and generate dykes above 50 km to provide melt to shield volcanoes.

113x182mm (300 x 300 DPI)

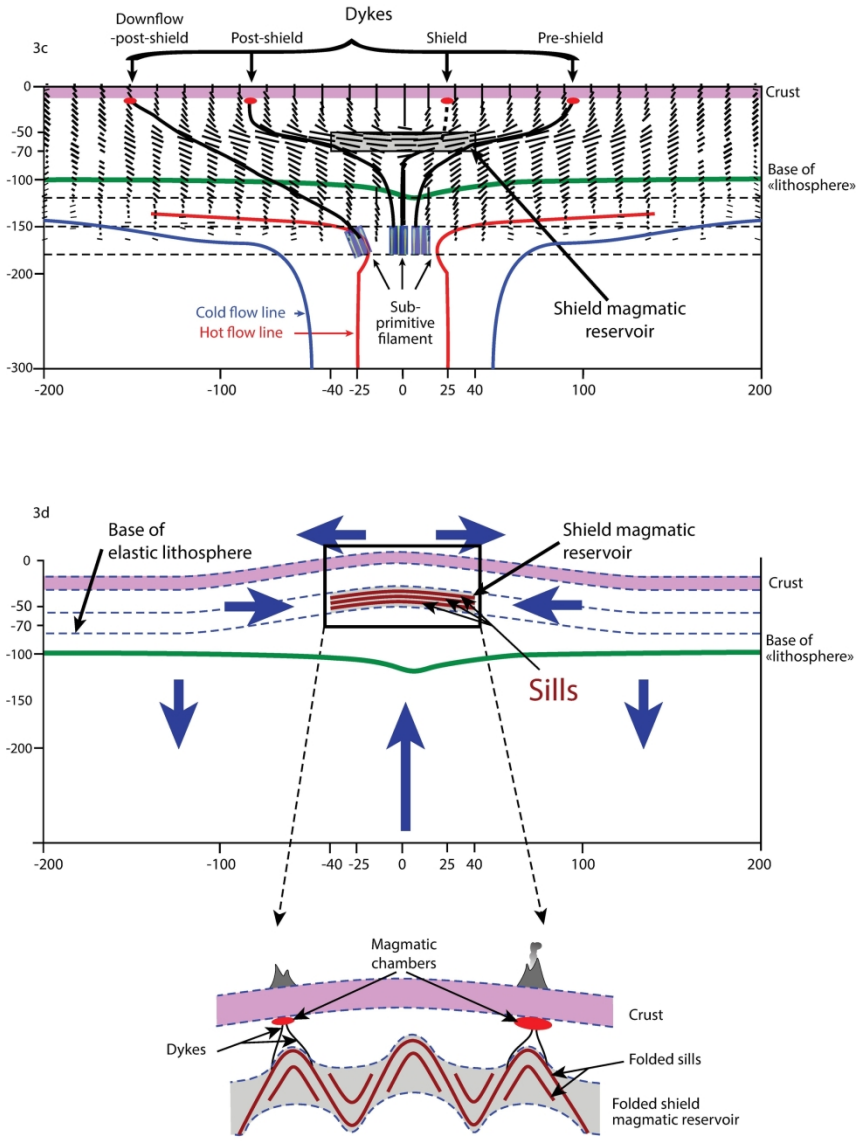

Fig. 3c and d

189x267mm (300 x 300 DPI)

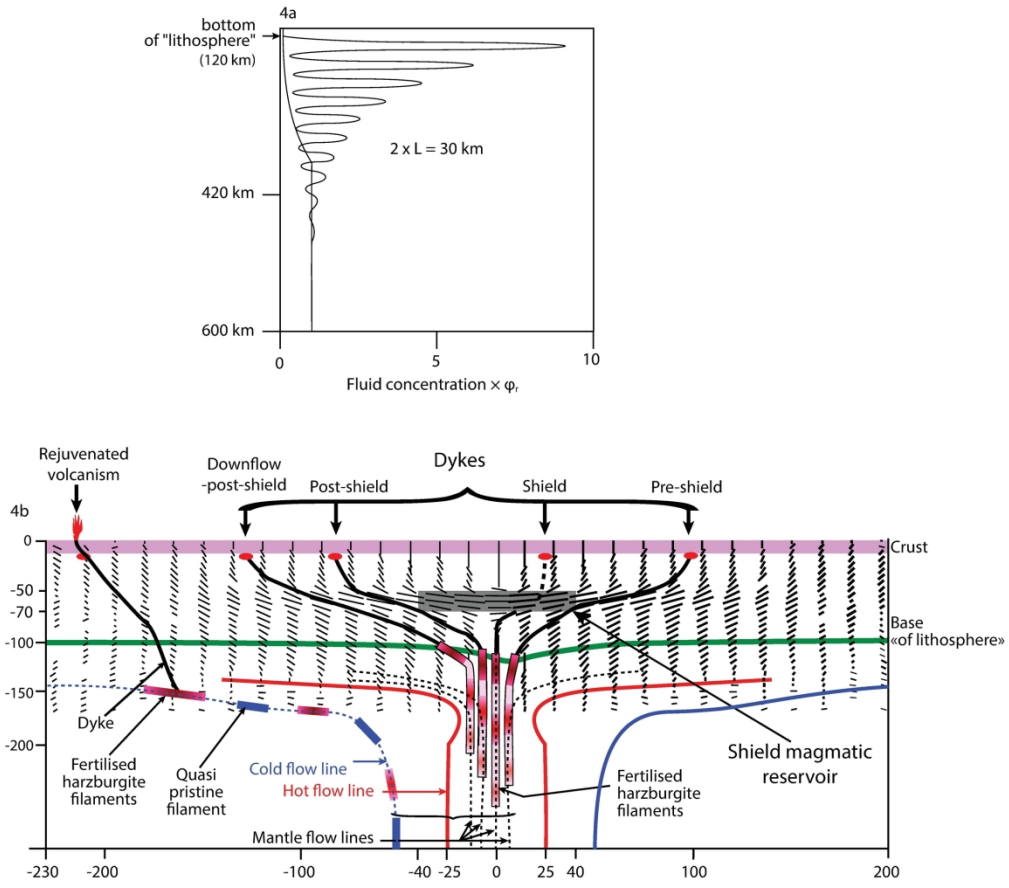

Fig. 4 Evolution (1D) of melt concentration related to the obstruction of upward melt percolation, which occurs at the bottom of the lithosphere (from Rabinowicz & Ceuleneer, 2005). The initial melt concentration profile of the computation is drawn in a thin plain line, above 420 km depth, where it is equal to ϕr, the initial melt/mush mass ratio. The bold plain line represents the evolution of melt concentration after 80 ka. Note that below the lithosphere, the uppermost compaction wave is ~30 km thick and reaches a maximum melt concentration of ~10ϕr. b) The trajectories of the dykes that develop at the top of the compaction waves and in which carbonatite/kimberlite-like melts are concentrated. This process stems from the dehydration and decarbonation of the fertilized-harzburgite filaments above the mantle transition zone (see text). The intensity of interstitial melt concentration is represented by the colour gradient from intense red to light pink. Along the plume axis, a train of compaction waves develops because of the permeability drop at the base of the lithosphere. Away from the plume axis, in contrast, a train of compaction waves results from the horizontalization of flowlines due to the rotation of the flow below the lithosphere (see text). Inside the hot centre of the plume, the mantle in the upper wave melts completely to form meimechite-like melts that apply a pressure at the plume top to trigger dykes that follow the direction of σ1 to transport the melt

up to the base of the crust. The trajectories are very similar to those of sub-primitive filaments (Fig. 3) and thus feed the same volcanoes. Similarly, along the elbow formed by the cold flowline, carbonatitic melt may accumulate; however, because of the low temperature, fertilized-harzburgite filaments only experience moderate partial melting. The produced melt is channelled along the weakly tilted (to horizontal) arm of the elbow. The resulting kimberlite-like melt concentrates at its apex, where excess pressure is sufficient to promote melt transport via dykes up to the subcrust or even to the surface at a distance >200 km from the plume axis. This process explains rejuvenated volcanism (see text).

204x238mm (300 x 300 DPI)

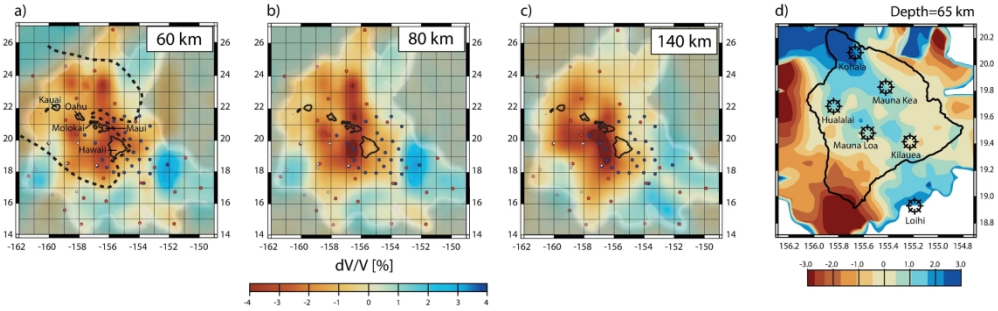

Fig. 5 Vp seismic anomalies (in %), derived from the Rayleigh wave tomographic model of Laske et al. (2012), at a) 60 km, b) 80 km and c) 140 km depth. d) Vp seismic anomalies (in %) at 65 km depth, as derived from the P-volume wave tomography model of Tillman et al. (2001). Note that the seismic anomalies are positive and represent local maxima above both the main island and the main shield volcanoes.

216x65mm (300 x 300 DPI)

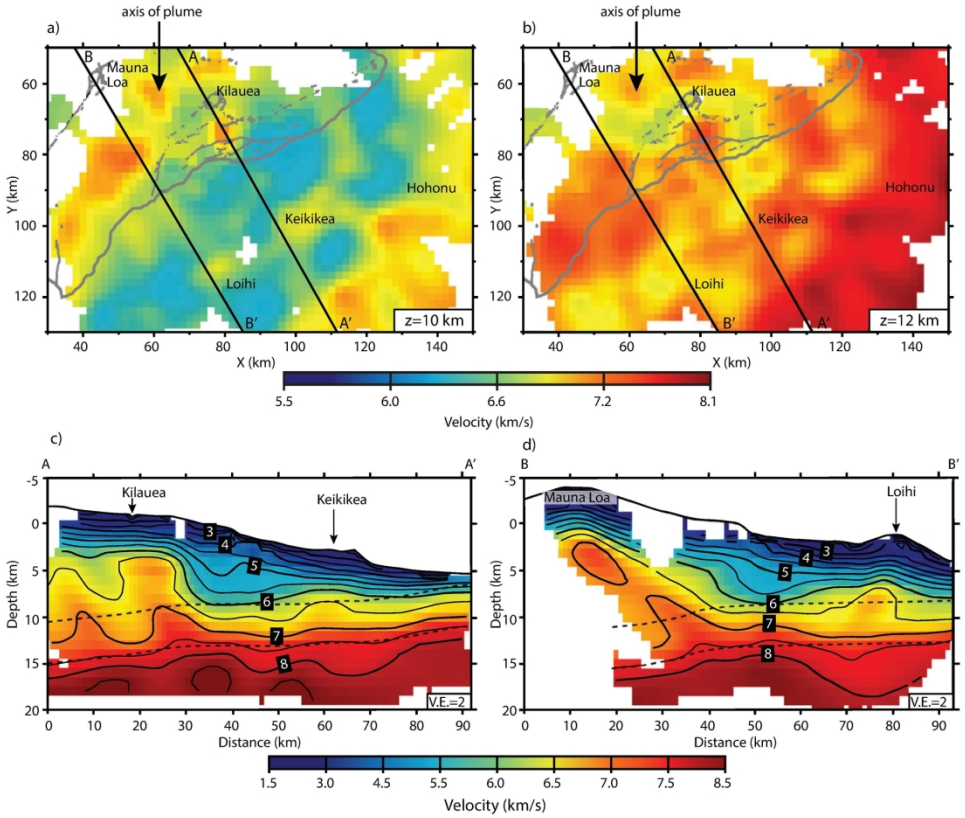

Fig. 6 Three-dimensional onshore–offshore Vp seismic tomography of the eastern margin of the main island (from Park et al., 2007), with velocity fields at a) 10 km and b) 12 km depth. A velocity <6 km/s corresponds to crustal material, whereas a velocity >6 km/s corresponds to mafic or mantle materials. Also provided are the vertical velocity fields along the profiles c) AA′ (in Fig. 6a) and d) BB′ (in Fig. 6b). The positions of Mauna Loa, Loihi, Kilauea, Keikikea and Hohonu are indicated.

170x139mm (300 x 300 DPI)

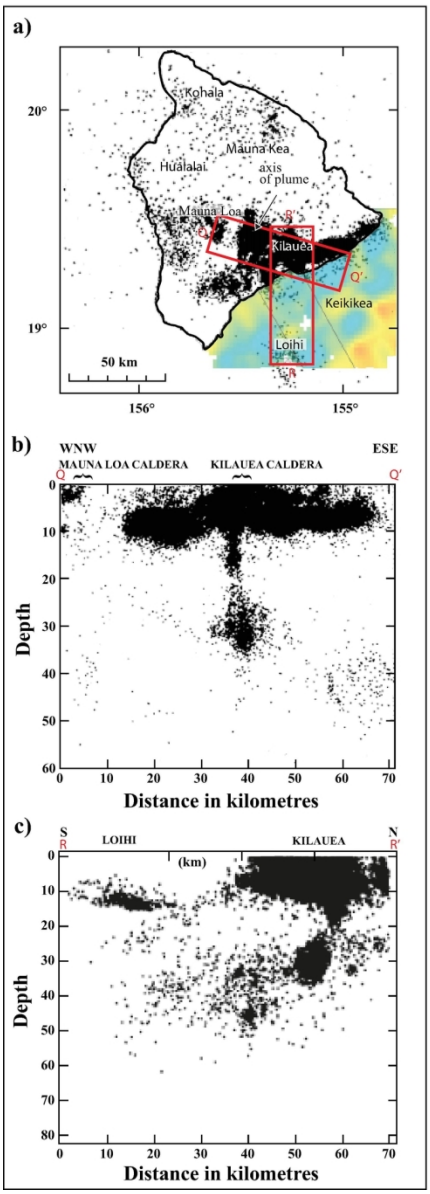

Fig. 7 a) Representation of the surface distribution of the loci of various earthquakes around the main island (from Tillman et al., 2001). The Vp-anomaly map at 10 km depth identifies the location of Lohihi and Keikikea volcanoes and associated seismic activity (the full map is displayed in Fig. 6a). Also provided is the distribution of the loci of earthquakes along a vertical plane linking b) Mauna Loa to Kilauea (Tillman et al., 2001) and c) Loihi to Kilauea (Klein, 1982).

129x184mm (300 x 300 DPI)

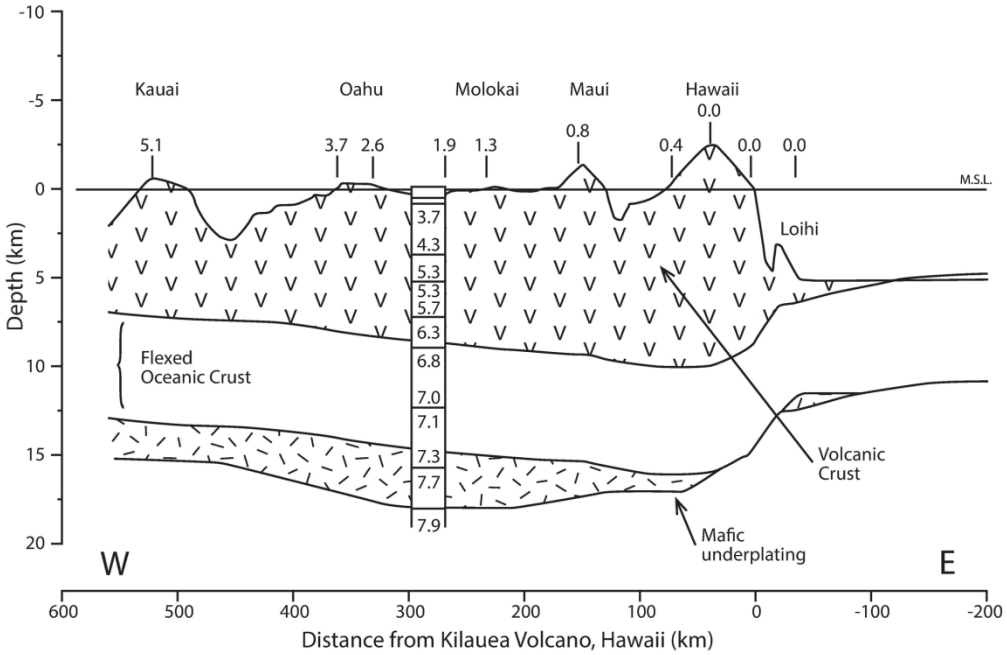

Fig. 8 Model of Watts & ten Brink (1989) of the evolution of the Moho depth along the Hawaiian chain, including topography, positions of the top of the oceanic crust, base of the oceanic crust and depth of the Moho discontinuity along the axis of the Hawaiian chain. The numbers above the islands are the radiogenic ages of surface lavas (Clague & Dalrymple, 1987). The velocity–depth structure based on ESP 5 is also presented (ten Brink & Brocher, 1988).

183x119mm (300 x 300 DPI)

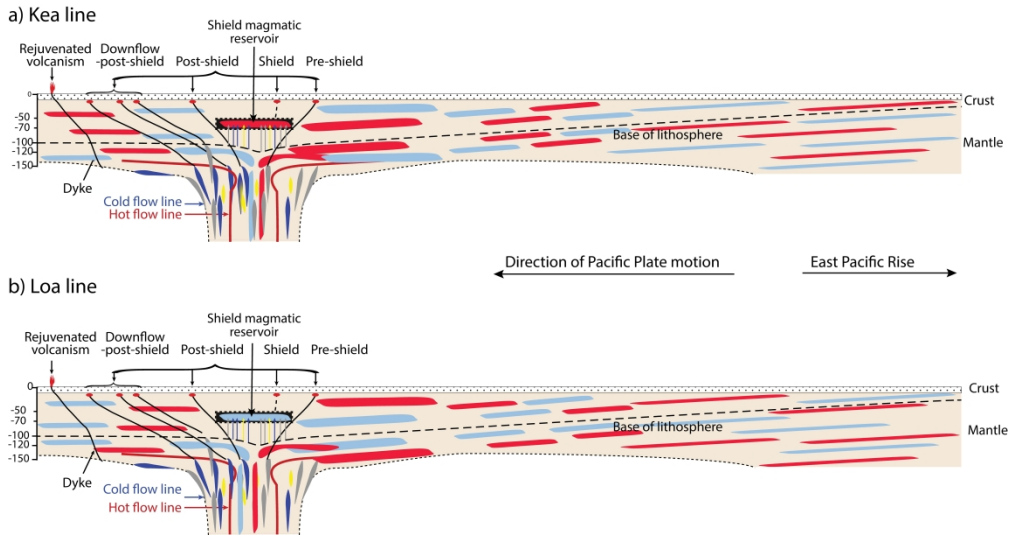

Fig. 9 Diagrams illustrating the flow of various mantle materials of the Hawaiian plume along the Mauna Kea and Mauna Loa lines. The basic flow (cream color) is assumed to consist of dry peridotite; the light blue stripes represent devolatized LLSVP mantle, i.e. Loa-type mantle, and the red stripes represent devolatized Pacific, i.e. Kea-type mantle. Sub-primitive/ULVZ (deep blue), eclogite (yellow) and fertilized-harzburgite (grey) filaments are transported by the mantle flow and eventually partially melt beneath the lithosphere. The melts provided by filaments are collected in dykes rooting between 120 and 150 km depth and are eventually transported upward to pond in the shield reservoir and subcrustal magma chambers (preshield, postshield and downflow-postshield dykes) or directly erupt at the surface (rejuvenated dykes). It is important to note that the type of mantle composing the lithosphere depends on its nature when it was integrated to the lithosphere during its subsidence, i.e., far from the present position of the plume. Because the type of mantle in the shield magma reservoir determines the Kea (light blue) or Loa (dark pink) nature of shield magma, it is deduced that, at present, the nature of the mantle within the shield reservoir and the sublithospheric plume flow is identical. This is not the case downflow of the plume, however, where the nature of mantle sources of shield melts fluctuates along both lines.

628x334mm (300 x 300 DPI)